**Imaging analysis of six human histone H1 variants reveals universal enrichment of H1.2, H1.3, and H1.5 at the nuclear periphery and nucleolar H1X presence**

**Mónica Salinas-Pena[1], Elena Rebollo[1], Albert Jordan[1,*]**

[1]Molecular Biology Institute of Barcelona (IBMB-CSIC), Barcelona, 08028, Spain

*To whom correspondence should be addressed. Tel: +34 93 402 0487; Fax: +34 93 403 4979; Email: Albert.jordan@ibmb.csic.es

Running title: **Differential nuclear distribution of human H1 variants**

**Abstract**

Histone H1 participates in chromatin condensation and regulates nuclear processes. Human somatic cells may contain up to seven histone H1 variants, although their functional heterogeneity is not fully understood. Here, we have profiled the differential nuclear distribution of the somatic H1 repertoire in human cells through imaging techniques including super-resolution microscopy. H1 variants exhibit characteristic distribution patterns in both interphase and mitosis. H1.2, H1.3, and H1.5 are universally enriched at the nuclear periphery in all cell lines analyzed and co-localize with compacted DNA. H1.0 shows a less pronounced peripheral localization, with apparent variability among different cell lines. On the other hand, H1.4 and H1X are distributed throughout the nucleus, being H1X universally enriched in high-GC regions and abundant in the nucleoli. Interestingly, H1.4 and H1.0 show a more peripheral distribution in cell lines lacking H1.3 and H1.5. The differential distribution patterns of H1 suggest specific functionalities in organizing lamina-associated domains or nucleolar activity, which is further supported by a distinct response of H1X or phosphorylated H1.4 to the inhibition of rDNA transcription. Moreover, H1 variants depletion affects chromatin structure in a variant-specific manner. Concretely, H1.2 knock-down, either alone or combined, triggers a global chromatin decompaction. Overall, imaging has allowed us to distinguish H1 variants distribution beyond the segregation in two groups denoted by previous ChIP-seq determinations. Our results support H1 variants heterogeneity and suggest that variant-specific functionality can be shared between different cell types.

## Introduction

The eukaryotic genome is organized in a functional and spatially segregated manner within the interphase nucleus. Nuclear architecture plays a crucial role in gene regulation and defining cellular identity. Early studies led to the classical view of a bipartite chromatin composition in which euchromatin is defined as active chromatin located at the nuclear center while heterochromatin corresponds to the more compact chromatin fraction, generally positioned at the nuclear periphery and surrounding the nucleoli (Cremer and Cremer, 2001; Jost et al., 2012; Solovei et al., 2016). While heterochromatin correlates with late-replicating, low-GC chromatin, euchromatin is characterized by an early replication timing and high-GC content. This differential epigenetic landscape of the interphase nucleus can be also recapitulated by Giemsa bands (G-bands) (Serna-Pujol et al., 2021), which arise from the characteristic banding of metaphase chromosomes.

Chromatin organization involves several hierarchical levels, including chromosome territories (Cremer and Cremer, 2001; Girelli et al., 2020), A (active) and B (inactive) compartments at the megabase level (Lieberman-Aiden et al., 2009), topological associated domains (TADs) (Dixon et al., 2012; Nora et al., 2012; Sexton et al., 2012) and chromatin loops. Moreover, chromatin segregation is facilitated by chromatin tethering to scaffolding structures. This anchorage originates nuclear environments referred as lamina-associated domains (LADs) or nucleolus-associated domains (NADs), which constitute heterochromatic regions anchored to the nuclear lamina and the nucleolus, respectively.

Human cells have 1000-1500 LADs that cover more than one-third of the genome (Guelen et al., 2008). LADs represent a well-known repressive environment, characterized by low gene density, low gene expression and a great overlap with B compartment. LADs are enriched in repressive histone modifications, including H3K9me2, which is considered a conserved chromatin mark of LADs (Poleshko et al., 2019). While H3K9me2 plays a part in anchoring chromatin to the nuclear lamina, current data indicates that it is probably not a sufficient signal in mammals, as other anchoring mechanisms may exist (Harr et al., 2015; Kind et al., 2013).

The nucleolus is a membraneless structure where ribosome biogenesis and regulation occurs. Nucleoli also act as central chromatin organizers. Genomic regions positioned close to nucleolus are referred as NADs, which were firstly genome-wide identified in human using a biochemical purification of nucleoli (Dillinger et al., 2017; Nemeth et al., 2010). NADs consist of mainly heterochromatic regions and an important overlap with LADs was found. Accordingly, some LADs have been found to stochastically reshuffled after mitosis and associate with nucleoli (Kind et al., 2013). These observations suggest that the lamina and nucleolus could act as interchangeable scaffolds for heterochromatin positioning. More recently, the inclusion of HiC-based approaches has

provided more accurate genome-wide NADs maps (Bersaglieri et al., 2022; Peng et al., 2023).

Histone composition, including histone variants and their modifications, also plays a role in defining chromatin functionality (Martire and Banaszynski, 2020). In particular, linker histone H1 family is evolutionary diverse and human somatic cells may contain up to seven H1 variants (H1.1 to H1.5, H1.0 and H1X). Although H1 has classically been regarded as a general repressor, increasing evidence support H1 variants functional diversity in chromatin regulation (Fyodorov et al., 2018; Millán-Ariño et al., 2016). A compromised H1 content causes chromatin structural defects, evidenced both in human (Serna-Pujol et al., 2022) and mice models (Geeven et al., 2015; Willcockson et al., 2021; Yusufova et al., 2021). Although in these scenarios multiple H1 variants depletion leads to chromatin decompaction, the contribution of individual H1 variants in maintaining chromatin structure has not been studied.

A long-standing enigma concerning H1 is whether its variants have a uniform distribution in different cell types or, conversely, display cell-line-specific binding patterns. The presumption that H1 variants are specifically distributed among different cell lines comes from combining various pieces of evidence from different publications (Cao et al., 2013; Izzo et al., 2013; Li et al., 2012; Millán-Ariño et al., 2014; Morales-Torres et al., 2016). Nevertheless, no study has properly addressed the question up to date. Consequently, the absence of existing reports using standardized experimental and analytical workflows may lead to potential misinterpretation of the data. The only studies that performed a systematic analysis of different variants have been performed in a single cell model and often used overexpression strategies. These include the analysis of H1.1-H1.5 using DamID in IMR-90 cells (Izzo et al., 2013), and a second report in which ChIP-Seq of endogenous H1.2 and H1X and the exogenous H1.0-HA and H1.4-HA was performed in T47D cells (Millán-Ariño et al., 2014). Recently, we performed the first genome-wide analysis of six endogenous H1 variants in human cells, bypassing the everlasting limitation of mapping exogenous proteins ((Serna-Pujol et al., 2022) and in preparation for H1.3 data). In T47D cells, H1 variants are distributed in two large groups depending on the local GC content. H1.2, H1.3, H1.5 and H1.0 are enriched at low-GC regions and B compartment while H1.4 and H1X are more abundant within high-GC regions and A compartment. However, whether these distribution profiles are conserved among different cell types remains unknown.

H1 complement (i.e. H1 variants and its proportions present in a specific cell) is dynamic throughout differentiation and cancer and also varies between cell types. Whether these expression fluctuations translate into changes in distribution patterns has not been studied. The best-characterized example is H1.0, which accumulates during differentiation (Terme et al., 2011) and whose expression is associated to a less aggressive phenotype of tumoral cells (Morales-Torres et al., 2016). H1.0 has been described as a replacement histone, as it responds to a compromised H1 content. In

breast cancer cells, combined depletion of H1.2 and H1.4 leads to H1.0 upregulation, although without significant redistribution alterations (Izquierdo-Bouldstridge et al., 2017; Serna-Pujol et al., 2022).

In this study, we provide novel insights into the differential nuclear distribution of somatic H1 variants in human cells, through an imaging approach. Super-resolution microscopy in T47D cells shows that H1.2, H1.3, H1.5 and, to a lesser extent, H1.0, are enriched at the nuclear periphery and coincide more with more compacted DNA, as supported by super-resolution microscopy. Contrarywise, H1X and H1.4 are distributed throughout the nucleus with a significant H1X enrichment in nucleoli. Differential distribution patterns suggest concrete implications in genome functionality and translate into variant-specific functional consequences upon H1 depletion. Specifically, single or combined H1.2 depletion triggers a general chromatin decompaction, which is not observed when depleting H1.4 or H1X. Furthermore, we conducted the first systematic comparison of six somatic H1 variants in several human cell lines, including ChIP-Seq profiling of H1X in different cell types, which has only been mapped in T47D breast cancer cells up to date. Interestingly, certain H1 variants display universal distribution patterns, despite variations in H1 complement across cell lines. H1.2, H1.3 and H1.5, are consistently enriched at the nuclear periphery while H1X is more abundant at high-GC regions and present at nucleoli in all cell lines evaluated. We identified a recurring concomitant absence of H1.3 and H1.5, and this specific H1 complement is associated with a more peripheral distribution of H1.0 and H1.4 proteins, suggesting potential compensatory mechanisms between variants. Altogether, our study represents a comprehensive attempt to systematically characterize the repertoire of somatic H1 variants, their differential distribution in the human genome and their functional diversity.

## Material and Methods

### Cell lines, culturing conditions and H1 variants knock-downs

Breast cancer T47D-MTVL derivative cell lines, which carry one stably integrated copy of luciferase reporter gene driven by the MMTV promoter, were grown in RPMI 1640 medium, supplemented with 10% FBS, 2 mM L-glutamine, 100 U/ml penicillin, and 100 µg/ml streptomycin, as described previously. SK-MEL-147, SK-MEL-173, UACC-257, SK-N-SH, HeLa, HCT-116, HT-29, CaCo-2, HepG2, 293T, NT2-D1, IMR-90 cell lines were grown in DMEM GlutaMax medium, supplemented with 10% FBS and 1% penicillin/streptomycin. IGR-39, SK-MEL-28, WM266-4 cell lines were grown in DMEM GlutaMax medium, supplemented with 10% FBS, 1% penicillin/streptomycin and 1% HEPES. MCF-7 cell line was grown in MEM medium containing 10% FBS, 1% penicillin/streptomycin, 1% non-essential aminoacids, 1% sodium pyruvate and 1% L-Glutamine. MDA-MB-231 cell line was grown in DMEM/F-12 medium containing 10% FBS, 1% penicillin/streptomycin and 1% L-Glutamine. All cell lines were grown at 37◦C with 5% $CO_2$.

Doxycycline (Dox)-inducible shRNA H1 knock-downs (KD) were described in previous works (Izquierdo-Bouldstridge et al., 2017; Mayor et al., 2015; Sancho et al., 2008). Concretely, T47D H1.4sh (Izquierdo-Bouldstridge et al., 2017) and T47D H1.2sh (Sancho et al., 2008) , T47D H1Xsh (Mayor et al., 2015), cell lines were used to analyze single H1 depletion. The T47D-MTVL multiH1 shRNA cell line (Izquierdo-Bouldstridge et al., 2017) was used as a model for H1 depletion. In multiH1 KD, combined depletion of H1.2 and H1.4 proteins occurs, although it reduces the expression of several H1 transcripts. A derivative cell line containing a Randomsh RNA was used as a control (Sancho et al., 2008).

### Drug treatments

shRNA expression was induced with 6-days treatment of Doxycycline (Dox), in which cells were passaged on day 3. Dox (Sigma) was added at 2.5µg/ml. 5-aza-2´-deoxycytidine (aza) was added at 5 µM for 3 days, in which medium was replaced at day 2 by fresh aza-containing medium. Actinomycin D (ActD) was added at 50 ng/ml for 24h. To study the distribution of H1 variants in mitosis by immunofluorescence in T47D, we performed Thymidine-Nocodazole synchronization, in order to increase the percentage of mitotic cells in the sample.

### Immunofluorescence

Cells were directly grown on glass coverslips (0.17mm thickness, 1.5H high-performance; Marienfeld Superior) placed in 24-well plates. Cells were fixed with 4% paraformaldehyde (20 min; RT), permeabilized with Methanol (10 min RT) and blocked with 5% bovine serum albumin (5% BSA diluted in PBS-Triton 0.1%). Primary antibodies of interest were incubated overnight at 4ºC. Secondary antibodies conjugated to Alexa

fluorophores were incubated 1h RT in the dark. The following conjugated secondary antibodies (Invitrogen) were used: goat anti-rabbit IgG H+L (Alexa 488 or 647); donkey anti-mouse IgG H+L (Alexa 555, 561, 633 or 647). After incubation, samples were washed with PBS-T (x3) and nuclei were stained with Hoechst (25 µg/ml diluted in 5%BSA-PBS-T; 1h RT in the dark). 5 PBS-T washes and a final MiliQ water were performed. Coverslips were mounted using Pro-long glass (Invitrogen). Preparations were maintained 24-48h in the dark at RT and then stored at 4ºC up to image acquisition.

**Image acquisition**

All images were acquired in a *Dragonfly 505* multimodal spinning-disk confocal microscope (Andor Technologies, Inc), using a 100x/NA-1.49 Apochromat oil immersion objective, a sCMOS Andor Sona 4.2B-11 camera and Fusion acquisition software. Pinhole diameter 40 µm were used for confocal imaging. Laser excitation was done sequentially. Alexa-633 and Alexa-647 were excited by 647-nm laser, Alexa-555 and Alexa-561 were excited by 561-nm laser, Alexa-488 was excited by 488-nm laser and Hoechst was excited by 405-nm laser. Exposure time and laser intensity were adapted in each case, ensuring the absence of saturating pixels. 16-bit images were acquired. Confocal 3D images were taken as Z-stacks with 0.11 µm intervals, with a voxel size of 51x51x110 nm. GPU-assisted deconvolution (Regularized Richardson-Lucy, 16 iterations) was applied after acquisition using the Fusion software. Deconvolved images are shown and representative confocal images show a single focal plane, unless indicated in the Figure legend.

Super-Resolution Radial Fluctuations (SRRF) algorithm (Culley et al., 2018; Gustafsson et al., 2016) was applied using the SRRF-Stream+ module (Andor) operated from the Fusion software. SRRF was performed for 1) co-localization experiments and 2) chromatin structure evaluation at extended resolution. For SRRF co-localization experiments a single Z confocal plane 1024x1024 was imaged. When evaluating H1 variants co-localization with DNA, H1 variants were labelled with Alexa-488 (except for H1.0, which was labelled with Alexa 561) and Hoechst was used for DNA staining. For H1 variants co-localization with H1.0, H1 variants were labelled with Alexa-488 and H1.0 with Alexa-561. Images frames were also acquired sequentially for each channel. The following parameters were used for all conditions: 1x ring radius, 6x radiality magnification (i.e. each pixel is magnified in an array of 6x6 sub-pixels), 500 frames. Exposure time 250ms and 18% laser intensity were used for 405-nm channel (Hoechst imaging). Exposure time 180-200 ms and 8-12% laser intensity were used for 488-nm or 561-nm channels. Under these conditions, pixel size corresponds to 8.5 nm (in x,y).

For evaluating DNA structure upon H1 KDs, SRRF imaging of DNA (Hoechst) was used. SRRF was performed on 1024x1024 wide-field images with the following parameters: exposure time 150ms, 10% 405-nm laser intensity, 1x ring radius, 6x radiality

magnification, 1000 frames. Under these conditions, pixel size corresponds to 8.5 nm (in x,y).

**Image analysis**

Image analysis was performed in ImageJ software. Data was post-processed and plotted in R or Excel. Fluorescence intensity quantification was done by generating masks for each nucleus using Hoechst signal as reference and computing the mean intensity of the proteins of interest. Alternatively, Corrected Total Cell Fluorescence formula was used and calculated as: Integrated Density - Area of selected nucleus x Mean fluorescence of background readings. Line signal intensity profile plots were created using Plot Profile tool. Analysis of ring intensity distribution was done with a macro available at https://github.com/MolecularImagingPlatformIBMB with minor modifications. Every nucleus is partitioned into four concentric rings with equal areas that converge towards the center of the nucleus. Subsequently, the signal intensity density of the specific interest is assessed for each ring and adjusted to the total intensity density of the nucleus. This approach enables the comparison of the intensity distribution of a target protein among nuclei varying in shape and size. Pearson´s correlation coefficient (r) was calculated using JaCoP Plugin. Calculation was done from a unique Z central plane in single nuclei and after channel thresholding. Co-localization in SRRF images was calculated with an in-house macro. Briefly, after pre-processing steps, it creates a mask of each channel and calculates the intersection between both masks of interest (in % of intersected pixels). To compare chromatin structure through DNA super-resolution in different H1 KD conditions, we used DNA-free areas method, which has been used elsewhere to assess DNA compaction (Martin et al., 2021; Neguembor et al., 2021). We constructed an interactive macro that allowed us to sample each nucleus using user-defined regions of interest (ROI) and then automatically calculates the free-DNA areas per ROI. For each nucleus, a number of ROIs (200x200 px) were drawn as to cover all the nuclear area, excluding nucleolus. Per each ROI, auto-local thresholding using the Phansalkar filtering algorithm was applied to the Hoechst channel. Based on this filtering, percentage of DNA-free areas was calculated.

**Histones extraction**

For isolation of total histones, cell pellets were resuspended in 1 ml of hypotonic solution [10 mM Tris–HCl (pH 8.0), 1 mM KCl, 1.5 mM MgCl2, 1 mM PMSF, 1 mM DTT] and incubated on ice for 30 min. The nuclei were pelleted at 10000 × g for 10 min at 4oC. Sulfuric acid (0.2 M) was added to the pellet to extract the histones on ice for 30 min. The solution was centrifuged at 16000 × g for 10 min at 4oC. TCA was added to the supernatant in order to precipitate histones. After >1h ice-incubation precipitate was centrifuged (16000xg 10 min at 4oC). Precipitate was washed with acetone and finally resuspended in water. Protein concentration was determined by Micro BCA protein assay (Thermo Scientific) and immunoblot was performed.

**Immunoblot**

Histone samples were exposed to SDS-PAGE (14%), transferred to a PVDF membrane, blocked with Odyssey blocking buffer (LI-COR Biosciences) or 5% non-fat milk for 1 h, and incubated with primary antibodies overnight at 4◦C as well as with secondary antibodies conjugated to fluorescence (IRDye 680 goat anti-rabbit IgG or IRDye 800 goat anti-mouse IgG, Li-Cor) for 1 h at room temperature. Bands were visualized in an Odyssey Infrared Imaging System (Li-Cor). Coomassie staining or histone H3 /histone H4 immunoblotting were used as loading controls. ImageJ software was used for immunoblot quantification.

**Antibodies**

Specific antibodies recognizing human H1 variants used for immunofluorescence, immunoblot and ChIP-Seq were: anti-H1.0/H5 clone 3H9 (Millipore, 05–629-I), anti-H1.2 (abcam, ab4086), anti-H1.3 (abcam, ab203948), anti-H1.4 (Invitrogen, 702876), anti-H1.5 (Invitrogen, 711912) and anti-H1X (abcam, ab31972). Other antibodies used in immunofluorescence and/or immunoblot were: H1.2-pT165 (H1.2 phosphorylated in Thr-165; Millipore 06-1370), H1.4-pT146 (H1.4 phosphorylated in Thr-146; ab3596), LaminA (ab8980), H3K9me2 (ab1220), NPM1 (ab10530), H3 (ab1791), H4 (ab10158). For immunoblots in **Figure 5-figure supplement 1**, H1.3 (ab24174) antibody was used. In **Figure 5-figure supplement 1A**, H1.0 immunoblot was performed with H1.0 (ab11079) antibody. Of note, anti-H1.4pT146 immunogen was a synthetic peptide derived from within residues 100–200 of human H1.4, phosphorylated at T146. However, this antibody could also recognize phosphor-T146 in H1.2, H1.3 (both 88% sequence identity with immunogen). Importantly, source of H1 variants antibodies limit co-immunostaining studies. All H1 variants antibodies are raised in rabbit, except for H1.0 antibody, which is raised in mouse.

**RNA extraction and reverse transcriptase (RT)-qPCR**

Total RNA was extracted using the High Pure RNA Isolation Kit (Roche). Then, cDNA was generated from 100 ng of RNA using the Superscript First Strand Synthesis System (Invitrogen). Gene products were analyzed by qPCR, using SYBR Green Master Mix (Invitrogen) and specific oligonucleotides in a QuantStudio 5 machine (Applied Biosystems). Each value was corrected by GAPDH and by the corresponding cell line genomic DNA amplification of each primer pair. Specific qPCR oligonucleotide sequences are listed in **Supplementary Table S1**.

**ChIP and ChIP-Seq**

All H1 ChIP-seq experiments were performed and analyzed as previously detailed (Serna-Pujol et al., 2022). ChIP-Seq replicates of H1.0, H1.2, H1.4, H1.5 and H1X in T47D cells from our previous publication (Serna-Pujol et al., 2022)are accessible through GEO Series accession numbers GSE156036 and GSE166645. Input-subtracted ChIP-Seq signal

was evaluated in genome segments of interest using BEDTools (Quinlan and Hall, 2010). Genome-wide GC content, Giemsa bands (G-bands) coordinates at 850 bands per haploid sequence (bphs) resolution and chromosomes coordinates were obtained from the UCSC human genome database (Karolchik et al., 2004; Navarro Gonzalez et al., 2021). G-bands were classified in eight groups as detailed in (Serna-Pujol et al., 2021): G-positive (Gpos25 to Gpos100, according to its intensity in Giemsa staining), and G-negative (unstained), which were further divided into four groups according to their GC content (Gneg1 to Gneg4, from high to low-GC content).

**Public data on H1 variants expression and H1 gene methylation**

H1 variants expression data and gene methylation in the NCI-60 cell lines panel was available at CellMiner (https://discover.nci.nih.gov/cellminer/) (Reinhold et al., 2019). Gene methylation data from Illumina 450K methylation BeadChip was expressed as β-values normalized to a value between 0 (unmethylated) and 1 (methylated). β -values from all identifiers (i.e. different probes) corresponding to the same H1 gene were considered and an average β-value was calculated per each H1 variant. Gene methylation in cancer patients from The Cancer Genome Atlas (TCGA) datasets was available at https://www.cbioportal.org/.

## Results

### Histone H1 variants are differentially enriched towards the periphery of the interphase nucleus and at nucleoli

We have recently reported that H1 variants are differentially distributed into two main groups within the genome of T47D cells: H1.0, H1.2, H1.3, H1.5 are enriched in low-GC regions while H1.4 and H1X are more abundant at high-GC regions (Serna-Pujol et al., 2022)(hereafter referred as "low-GC" or "high-GC" H1 variants). However, how these variants are distributed along the nucleus, where chromatin is spatially arranged to regulate genome function, remains unknown. Immunofluorescence analysis demonstrated that different H1 variants exhibit unique nuclear patterns (**Figure 1A**). H1.2, H1.3, and H1.5 were observed to be enriched at the nuclear periphery, while H1.0 was distributed throughout the nucleus, with certain enrichment territories that tend to be peripheral. On the other hand, H1.4 and H1X were found to be homogeneously distributed throughout the nucleus, with the difference that H1X was particularly abundant in the nucleoli. H1.2, H1.3, H1.5 and H1.0 showed a coincident pattern with DNA staining one, suggesting an enrichment at more condensed-DNA nuclear areas, including but not limited to the nuclear periphery (**Figure 1A**, bottom panels). H1.4 profile only partially mimicked DNA pattern while H1X profile was opposite to that of DNA. Overall, these results are compatible with the classification of H1 variants into two differential groups, as previously suggested by ChIP-Seq analysis, as low-GC chromatin tends to be peripheral and coincides with late-replicating heterochromatin.

To further examine H1 variants nuclear distribution, we performed an analysis of the H1 radial intensity distribution. Each nucleus was automatically divided into four sections of equal area (as exemplified in **Figure 1B**) and the percentage of H1 intensity present in each area was quantified (**Figure 1C**). H1.2, H1.3, and H1.5 showed a clear relationship with radiality, becoming increasingly abundant from the nuclear center to the periphery. Importantly, H1.0 was found to be most abundant at the two most peripheral percentiles. A different distribution was observed for H1.4, which was more equally distributed along A1-A4 sections, being more abundant at intermediate A2-A3 percentiles. H1X was gradually increasing towards the nucleus center. It is important to note that, in part, this gradual profile is due to the nucleolar H1X fraction, as nucleoli tend to be located at central nuclear positions and we are not excluding nucleoli from the analysis.

Differential H1 'radiality' is related to the spatial organization of chromatin in the nucleus of mammalian cells and the concept of chromosomes territories. Chromosomes are not randomly positioned in the nucleus; gene-poor chromosomes are located at peripheral positions while gene-rich chromosomes tend to occupy central regions (Boyle et al., 2001). We computed H1 variants ChIP-Seq abundance at chromosomes reported to occupy different radial territories **(Figure 1D)** and, supporting immunofluorescence

quantification, we found that H1.2, H1.3, H1.5 and H1.0 were enriched at peripheral chromosomes over central ones. On the contrary, H1.4 and H1X were more abundant at chromosomes located in central positions.

**Super-resolution imaging shows that low-GC H1 variants co-localize with compacted DNA and do not overlap**

We sought to extend the analysis to the super-resolution level. Super-resolution imaging techniques surpass the diffraction limit, enabling visualization of subcellular organization beyond conventional light microscopy resolution (≈250nm). Specifically, we used super-resolution radial fluctuations (SRRF) technique (Culley et al., 2018; Gustafsson et al., 2016). Super-resolution imaging of H1 variants reinforced the different nuclear patterns already seen through confocal microscopy **(Figure 2A)**. H1.2, H1.3, H1.5 and to a lesser extent H1.0, were specially detected at the nuclear periphery, but SRRF imaging emphasized their presence throughout the entire nucleus, highlighting that these variants are not limited to the nuclear periphery. For its part, H1.4 discrete signals were found throughout the whole nucleus, excluding nucleoli. Conversely, nucleolar H1X was detected but super-resolution accentuated the presence of the non-nucleolar H1X-fraction, which was observed throughout the entire nucleus.

The percentage of co-localization of histone H1 variants and DNA signal detected by SRRF was calculated **(Figure 2B)**. Of note, DNA super-resolution imaging distinguishes between areas of densely packed DNA and areas with little or no DNA signal, compared to the typically blurred DNA signal resolved by confocal resolution. Consequently, the DNA we detected through SRRF imaging represents chromatin in a more condensed or closed state, relative to surrounding regions. H1.2, H1.3, H1.5 and H1.0 showed a higher degree of co-localization with DNA compared to H1.4 and H1X, with H1X showing the least colocalization. In summary, our super-resolution co-localization studies of H1 variants with DNA reinforced the differential nuclear patterns obtained at a conventional resolution. Moreover, SRRF imaging highlights that, although showing preferential relative enrichment to concrete nuclear regions, such as nuclear periphery or nucleoli, H1 variants are not restricted to those compartments.

To further characterize H1 variants patterns, we next studied how H1.0 co-localizes with the rest of H1 variants in single nuclei (**Figure 2C,D**, **Figure 2-figure supplement 1A-C**). Preferential co-localization of H1.0 with H1.2/H1.3/H1.5 over H1.4 and H1X was evident at confocal resolution (**Figure 2-figure supplement 1A-C**), suggesting that low-GC variants occupy similar nuclear territories and supporting ChIP-Seq profiling obtained when analyzing T47D cell population. However, at the super-resolution level all H1 variants co-localized poorly with H1.0, suggesting that they occupy different chromatin fibers (**Figure 2D**). This observation could be underlying the principles of nucleosome composition and 3D chromatin organization. Considering the dissimilarities observed between the standard and super-resolution approaches, results suggest that, in single-

cells, at least in more closed regions where H1.0/H1.2/H1.3/H1.5 are more abundant, H1 variants are not occupying random positions in nearby nucleosomes. If that were the case, co-localization between the different 'low-GC' variants (*versus* 'high-GC' ones) would not be lost when improving resolution. Therefore, a compatible model with our results is that, in single cells, heterochromatic 3D-nanodomains tend to be consistently marked by a certain H1 variant.

**Attachment of H1 to mitotic chromosomes differs between variants**

As H1 variants showed different nuclear patterns in interphasic cells, we studied whether these differential patterns were also observed through mitosis **(Figure 2E)**. Co-immunostaining of replication-independent H1.0 and H1X was performed and their distribution through consecutive phases of mitosis was monitored **(Figure 2-figure supplement 2A)**. H1.0 and H1X exhibited completely different distribution patterns. While H1.0 was anchored to mitotic chromosomes, H1X was not recruited to mitotic chromosomes and it accumulated to the perichromosomal region.

H1 variants highly enriched at nuclear periphery during interphase were co-examined with LaminA along mitotic progression **(Figure 2-figure supplement 2B-D)**. Since nuclear lamina is disassembled during mitosis, we wondered whether the positional information of H1-marked chromatin was maintained through mitosis. H1.3 and H1.5 showed similar distribution profiles throughout mitosis **(Figure 2-figure supplement 2B, C)**. Both H1 variants persisted at mitotic chromatin, being specially enriched at the periphery of condensed chromosomes. Importantly, H1.3 and H1.5 layers re-associate with the forming nuclear lamina before mitotic exit. Instead, H1.2 signal was dispersed after prophase **(Figure 2-figure supplement 2D)**. H1.2 was re-detected at anaphase, when its peripheral enrichment was re-acquired, parallel to lamina re-assembly. These results suggest that radial position of H1.2, H1.3 and H1.5-marked chromatin is inherited through mitosis. These genomic regions are re-localized to the nuclear periphery following mitotic division and the nuclear lamina reassembles around H1.2, H1.3 or H1.5-associated chromatin.

The apparent absence of H1.2 (and H1.4, data not shown) at intermediate mitotic stages is striking. H1 proteins are highly phoshphorylated during mitosis, so we explored whether apparent mitotic absence was due to these H1 variants becoming highly post-translationally modified during mitosis, and the antibodies are not recognizing the H1-modified fraction. H1.2 Phosphorylation of Threonine 165 (H1.2-pT165) and H1.4 phosphorylation of Threonine 146 (H1.4-pT146) were found to be highly increased in mitosis compared to interphase **(Figure 2-figure supplement 3A)**. Thus, this confirms that H1.2 and H1.4 proteins are not absent at certain mitotic phases, but antibodies are unable to recognize their post-translationally modified state. Although these modifications are most prevalent in mitosis, they are also detected at interphase. Early-mitotic H1.2pT165 was found to be associated with condensed chromosomes, with

maximum levels occurring at metaphase and drastically dropping down at later mitotic phases **(Figure 2-figure supplement 3B)**. These temporal dynamics coincide with the previously discussed lack of H1.2 detection at metaphase and the re-appearance of H1.2 signal at anaphase/telophase **(Figure 2-figure supplement 2D)**. Furthermore, H1.4-pT146 was also more enriched at early mitotic stages, but excluded from metaphasic chromosomes **(Figure 2-figure supplement 3C)**. Instead, H1.4-pT146 was accumulated adjacent to chromosomes, in the perichromosomal layer, similar to what was observed for H1X **(Figure 2-figure supplement 2A).**

Overall, analysis of H1 variants during mitosis indicates that the two H1 groups defined by ChIP-Seq analysis present distinct localization patterns through mitosis. While 'low-GC' H1s (whether phosphorylated or not) are associated with mitotic chromosomes, 'high-GC' variants (phosphorylated or not) are excluded from mitotic chromosomes and accumulate to the perichromosomal region. In addition, H1.3 and H1.5 are enriched towards the peripheral chromosome regions, in comparison to H1.0 or H1.2-pT165. In conclusion, imaging experiments support the differential distribution of H1 variants not only during interphase but also in mitotic cells.

**H1.2, H1.3 and H1.5 are enriched within LADs**

Genome conformation is regulated by the tethering of chromatin to scaffold structures, such as the nuclear lamina or nucleolus. Several domains have been implicated in chromatin organization, such us LADs or NADs. Proper chromatin organization is crucial for genome functionality, so we further explored H1 variants differential distribution within these particular chromatin domains.

As H1.2, H1.3 and H1.5 were highly enriched at nuclear periphery **(Figure 1A, Figure 2)** and re-associated to lamina before mitotic exit **(Figure 2-figure supplement 2B-D)**, we aimed to explore their association with lamina through super-resolution microscopy **(Figure 3A)**. Interestingly, in all three cases, the peripheral H1 enrichment seen by confocal microscopy was perfectly resolved by SRRF imaging as an H1 layer adjacent to LaminA layer. We next performed H1 variants co-immunostaining with H3K9me2, an evolutionarily conserved specific mark of LADs (Poleshko et al., 2019). As expected, H3K9me2 was found enriched but not limited to nuclear periphery **(Figure 2-figure supplement 3A)**. Indeed, H3K9me2 nuclear pattern resembled the distributions of H1.2/H1.3 and H1.5 and a high co-localization was observed at both confocal **(Figure 3B, Figure 3-figure supplement 1A)** and SRRF resolutions **(Figure 3C)**.

As aforementioned, H1.0 was also found to be partially enriched at nuclear periphery **(Figure 1A,B)**. Taking advantage of publicly available LADs coordinates, we computed H1 variants ChIP-Seq abundance in LADs **(Figure 3D)**. 'Low-GC' H1 variants, including H1.0, were enriched at LADs in comparison to H1.4 and H1X. On the whole, we demonstrated that H1.2/H1.3/H1.5, and also H1.0, are constituents of lamina-associated chromatin, as supported by microscopic and ChIP-Seq experiments.

**H1X and phosphorylated H1.2 or H1.4 present differential nucleolar patterns**

We previously identified H1X enriched at nucleolus, using both confocal and super-resolution microscopy **(Figure 1, 2)**. To begin with, nucleolar H1X enrichment was found using alternative permeabilization methods (data not shown) and both nucleolar and non-nucleolar signals were drastically reduced upon specific H1X depletion **(Figure 3-figure supplement 1B)**, confirming that nucleolar H1X enrichment is not an artifact. Co-immunostaining of H1X and the nucleolar marker nucleophosmin (NPM1) confirmed that H1X was located inside nucleoli, with a tendency to form a ring-like layer adjacent to NPM1 on the inner side of nucleoli **(Figure 3E, F)**.

Nonetheless, H1X was not the only H1 variant present at nucleoli, as H1.2-pT165 and H1.4-pT146 were also present at nucleoli **(Figure 3F, Figure 2-figure supplement 3B, C)**. While interphasic H1.2-pT165 was highly enriched within nucleoli, interphasic H1.4-pT146 was not restricted to nucleoli, as it was also detected within the rest of the nucleus, specially coinciding with DNA-free staining regions. H1.4-pT146 formed clusters of punctate nucleolar staining. These characteristic nucleolar dots seem to represent active ribosomal DNA (rDNA) transcription, resembling immunostaining patterns of active rDNA transcriptional machinery factors (ie: UBF, RNApol I). A second interphasic H1.4-pT146 pattern was observed **(Figure 3-figure supplement 1C)**, with no nucleolar enrichment but speckled enrichment territories along the nucleus that overlap with regions with less DNA staining, i.e., less condensed chromatin. This speckled staining could represent the localization of transcriptionally active chromatin near RNA splicing factories, as has been proposed before for H1.4-pS187, which display an analogous interphasic staining (Zheng et al., 2010).

Next, we tested whether the nucleolar localization of H1 variants depends on nucleolar integrity, by treating cells with the rDNA transcription inhibitor Actinomycin D (ActD). ActD treatment triggers large-scale structural reorganization of the nucleoli, with the migration of some nucleolar markers to the nucleolar-remnant periphery, forming the so-called nucleolar caps while other nucleolar proteins are translocated to nucleoplasm (Burger et al., 2010). Each nucleolar cap represents UBF-loaded rDNA repeats from a single nucleolar organizer region (NOR). As expected, ActD treatment triggered a total translocation of NPM1 to nucleoplasm and alterations in DNA distribution were also evident **(Figure 3-figure supplement 1D)**. H1.4-pT146 was redistributed to the nucleolar caps, as it would be expected from active rRNA transcription machinery components. Nucleolar enrichment of H1.2-pT165 was completely lost upon ActD treatment, and it was not detected at nucleolar caps. However, the H1X characteristic nucleolar ring was still found in the remnant nucleoli of a considerable fraction of cells. Thus, H1X and phosphorylated-H1.2 or H1.4 exhibit characteristic nucleolar patterns, basally and upon ActD treatment, that could reflect different functional involvements in nucleolar dynamics.

We further explored H1 variants relationship with nucleolar organization by analyzing ChIP-Seq H1 variants abundance within NADs. We used a recently-published NADs mapping performed in HeLa cells, which identified 264 NADs (Peng et al., 2023). As NADs and LADs show a substantial overlap, we analyzed separately those regions defined exclusively as NAD or LAD and those that overlap (NAD/LAD), similar to the analysis performed in (Bersaglieri et al., 2022). 'Low-GC' H1 variants were enriched within both NADs and LADs, highlighting their presence within multiple repressive compartments in the nucleus. On the contrary, 'high-GC' H1 variants are depleted from both NADs and LADs repressive domains, compared to the A compartment **(Figure 3D)**. Still, H1X and H1.4 are more abundant at regions that are only classified as NADs (NADs-only) than NAD/LAD genomic regions, contrary to low-GC H1s.

**Single or combined H1.2 depletion leads to chromatin decompaction**

Due to the intrinsic link of chromatin compartmentalization and genome structure and the differential H1 variants abundance within those compartments, we examined how H1 depletion affects chromatin organization. Using super-resolution imaging of DNA we were able to visualize the chromatin structure **(Figure 4-figure supplement 1A)**. We performed super-resolution imaging of DNA under different H1 **(Figure 4A, Figure 4-figure supplement 1B)**. MultiH1 KD (i.e. simultaneous depletion of H1.2 and H1.4, see (Izquierdo-Bouldstridge et al., 2017)) led to a general disruption of chromatin organization compared to control conditions. This disruption was also evident, albeit to a lesser extent, upon single depletion of H1.2. In contrast, single depletion of H1.4 or H1X did not appear to produce changes in chromatin architecture at the level studied. To quantify chromatin structural changes upon H1 depletion, we used DNA-free areas analysis, as reported elsewhere (Martin et al., 2021; Neguembor et al., 2021). This method relies on the fact that DNA signal accumulates in densely packed areas. This leads to the appearance of areas with no DNA signal or low-density DNA signal (referred to as DNA-free areas). Considering this, upon DNA decompaction, a decrease in the percentage of DNA-free areas is expected. We quantified DNA-free areas under the different H1 KD conditions **(Figure 4B, Figure 4-figure supplement 1C)**. Thus, the percentage of DNA-free areas was strongly reduced upon multiH1 KD, supporting DNA decompaction. Similarly, H1.2 depletion also led to a decreased percentage of DNA-free areas, although the reduction was minor compared to multiH1 KD. Depletion of H1.4 or H1X did not lead to significant changes in % DNA-free areas. In conclusion, combined depletion of H1.2 and H1.4 but also single depletion of H1.2 have an impact on chromatin structure, leading to a general chromatin decompaction not seen when depleting other H1 variants.

**The nuclear distribution of H1 variants is mainly conserved among different cell lines with a full H1 complement but altered in cells with silenced H1.3/H1.5**

Total H1 content and the contribution of H1 variants to total H1 are known to vary among cell types but little is known about the comparative nuclear or genomic distribution of the H1 variants among cell types. To address H1 variants heterogeneity in human cells, we firstly investigated the protein content of H1 variants in different cell lines, most of which had a tumoral origin (**Figure 5-figure supplement 1A-D**). As previously reported, H1.2 and H1.4 were present in all tested cell lines (Lennox and Cohen, 1983; Meergans et al., 1997; Parseghian and Hamkalo, 2001; Piña and Suau, 1987). Notably, H1X was also universally-expressed. While H1.0 was only absent in HeLa cells, H1.3 and/or H1.5 proteins were not expressed in several cell lines (i.e. Hela, HepG2, HCT-116, HT-29, 293T, SK-MEL-173, IGR-39 and MDA-MB-231 (*data not shown*)). Specifically, we consistently found a simultaneous lack of both H1.3 and H1.5 (i.e. HCT-116, HT-29, SK-MEL-173, IGR-39). Interestingly, cell lines lacking H1.3 and H1.5 tend to have increased H1.0 levels compared to other cell lines tested. We also evaluated H1 variants mRNA expression levels by reverse-transcriptase-quantitative PCR (RT-qPCR) **(Figure 5-figure supplement 1E)**. H1.2 was the most expressed at mRNA level in all cell lines. Simultaneous absence of H1.3 and H1.5 seen at the protein level (**Figure 5-figure supplement 1A-D**) was also evident at the transcriptional level **(Figure 5-figure supplement 1E)**. For this reason, we next explored whether the concomitant repression of H1.3 and H1.5 may be mediated by DNA methylation. Analysis of NCBI-60 cell lines panel showed that H1.0, H1.1, H1.5, H1.3 expression levels exhibit a negative correlation with gene methylation status and they were not expressed in all cell lines **(Figure 5-figure supplement 2A)**. This observation indicates that in some cell lines, expression of these variants could be repressed by DNA methylation. Moreover, gene methylation data from cancer patients (TCGA) revealed that methylation of H1 variant genes varied between cancers originating from different tissues **(Figure 5-figure supplement 2B)**. H1.2, H1.4 and H1X genes were unmethylated in the three datasets analyzed, supporting their universal expression in human cells. On the other hand, gene methylation of the other H1 variants was variable.

We next explored whether transcriptional repression of H1 variants was reversed by inhibition of DNA methylation. In those cell lines lacking H1.3+H1.5, a huge mRNA upregulation of these variants occurred upon 5-aza-2'-deoxycytidine (aza) treatment **(Figure 5-figure supplement 2C)**. H1.0 expression was also upregulated in HeLa cells (which lack H1.0 protein) but to a lesser extent. Moreover, H1.1 expression was also upregulated upon aza treatment in all cell lines. Notably, H1.1 is not expressed basally in most cell lines **(Figure 5-figure supplement 1E)**. In summary, our analyses support that H1.3 and H1.5 could be repressed by DNA-methylation in a subset of cell lines.

To evaluate differential and common distribution patterns of H1 variants among different cell lines, we performed immunofluorescence of six endogenous H1 variants in some of the cell lines in which we characterized H1 complement **(Figure 5A,B)**. Importantly, H1.2/H1.3/H1.5 were universally enriched at the nuclear periphery, as

observed in T47D. H1.0 and H1.4 were distributed throughout the nucleus. Lastly, H1X was also distributed throughout the entire nucleus, but the intensity of its nucleolar enrichment was variable between cell lines.

As both H1.3 and H1.5 seemed to be universally enriched at LADs or peripheral chromatin, we investigated whether in cell lines lacking these two variants, re-distribution of the remaining H1 proteins to the nuclear periphery occurs. To do so, we performed H1 variants immunofluorescence in cell lines lacking H1.3 and H1.5 **(Figure 5B)**. In this subset of cell lines, H1.2 was also enriched at the nuclear periphery. Interestingly, H1.4 and H1.0 appeared to have a more peripheral distribution compared to cell lines expressing all H1 variants evaluated here. Indeed, we quantified H1.0 and H1.4 radial distribution (as exemplified in **Figure 1B**) and confirmed that those cell lines with a compromised H1 repertoire presented a more peripheral distribution of both H1.4 and H1.0, compared to those cell lines expressing all H1 variants **(Figure 5C, Figure 5-figure supplement 3A,B).** These results suggest that H1.0 and H1.4 balance H1 content at the nuclear periphery when H1.3 and H1.5 are absent, indicating that H1 levels are important to maintain peripheral chromatin, and, presumably, LADs.

We next focused our research on histone H1X. H1X was distributed throughout the whole nucleus in a punctuated pattern, with a variable nucleolar enrichment between different cell lines **(Figure 5A,B)**. Co-immunostaining of H1X with the nucleolar marker NPM1 confirmed H1X nucleolar enrichment **(Figure 5D)**. Among the cell lines tested, T47D, MCF-7, SK-MEL-147, HCT-116 and IMR-90 showed the most prominent H1X nucleolar enrichment. Notably, in MCF-7 breast cancer cells, H1X formed a layer at the nucleolar rim, adjacent to NPM1, similar to what was observed in T47D cells. Nevertheless, it is essential to note that H1X was still present at nucleoli in all cell lines tested, making it the H1 variant most associated with nucleoli, where other H1 variants are underrepresented.

Non-nucleolar H1X coincides with less-stained DNA regions, suggesting their enrichment at less compact chromatin. To further study H1X distribution, we performed H1X ChIP-Seq in several of the cell lines analyzed (i.e. SK-MEL-147, MCF-7, SK-N-SH, HeLa and HCT-116 and previously reported T47D). We used G-bands segmentation to compare the H1X ChIP-Seq abundance in the mentioned cell lines. H1X showed a strong correlation with %GC content in all cell lines, being highly enriched at high-GC G-bands **(Figure 5E).** Moreover, analysis demonstrates G-bands utility as epigenetic units to directly compare H1 variants binding profiles (Serna-Pujol et al., 2021).

Altogether, analysis of H1 variants distribution in different cell lines showed some universal features for certain variants. Concretely, H1.2, H1.3 and H1.5 are enriched towards the nuclear periphery in all cell lines tested. Interestingly, in cell lines lacking H1.3 and H1.5, H1.4 and H1.0 adopt a more peripheral distribution, suggesting a compensatory behavior. For its part, H1X is universally enriched at high-GC regions and

is the only H1 variant with evident presence within the nucleoli, although H1X nucleolar enrichment is variable among cell lines.

## Discussion

Tethering of chromatin to scaffold structures, such as the nuclear lamina or the nucleolus, regulates genome conformation and ultimately, its function. Despite being highly abundant proteins in the nucleus, distribution of histone H1 variants within nuclear domains has not been explored. We have recently reported that H1 variants exhibit differential genomic distributions in T47D breast cancer cells. H1.0, H1.2, H1.3 and H1.5 are enriched at low-GC regions and B compartment while H1.4 and H1X are more abundant within high-GC and A compartment regions (Serna-Pujol et al., 2022). Moreover, a combined depletion of H1.2 and H1.4 leads to chromatin decompaction at the level of TADs (Serna-Pujol et al., 2022), demonstrating that H1 proteins are involved in maintaining genome structure. In this study, we profiled the differential nuclear distribution of six somatic H1 variants in T47D cells and other human cells lines, through imaging techniques, including super-resolution microscopy. We provide here the first systematic comparison of H1 variants distribution in multiple human cell lines.

In T47D cells, H1.2, H1.3 and H1.5 and to a lesser extent H1.0 are enriched towards nuclear periphery. On the other hand, H1X and H1.4 are distributed throughout the nucleus with H1X being highly enriched in nucleoli (**Figure 1A**). Super-resolution imaging of H1 variants reinforced these differential profiles and revealed that H1.2/H1.3/H1.5/H1.0 coincide more with DNA pattern compared to H1.4 and H1X (**Figure 2A**), confirming their segregation in two groups denoted by ChIP-Seq data.

Emerging evidence from super-resolution microscopy indicates that nucleosomes are grouped in heterogenous nanodomains termed 'clutches' (Ricci et al., 2015). Moreover, topologically associated domains (TADs) represent structural chromatin folding units at the sub-megabase scale (Dixon et al., 2012; Nora et al., 2012; Sexton et al., 2012). We have shown that H1 variants form spatially separated nanodomains throughout the nucleus, visualized as a 'punctuate' signal by super-resolution imaging, but with the afore-mentioned differential variant-specific local enrichments. Similarly, super-resolution imaging of core histone H2B also present this clustered pattern in human fibroblasts (Ricci et al., 2015). It is important to mention that nucleosome clutches were originally defined using STORM technique (Ricci et al., 2015), whose resolution is higher than the one achieved by SRRF. For that reason, we favour the idea that nanodomains formed by H1 variants would be more equivalent to TADs or sub-TADs rather than to nucleosome clutches. In fact, shifts on the ChIP-Seq H1 variants distribution tend to coincide with TAD borders and H1 variants are more homogenous within the same TAD than between TADs (Serna-Pujol et al., 2021). This observation also highlights the relationship between H1 distribution and the structural properties of chromatin.

By conventional immunofluorescence, preferential localization of H1.0 with other 'low-GC' H1 variants over H1.4/H1X was observed **(Figure 2-figure supplement 1)**. However, this preferential colocalization was not evidenced at the super-resolution level and all

H1s colocalized similarly with H1.0 **(Figure 2B)**. This observation may suggest that domains spatially arranged at the 3D level are homogeneously marked by a certain H1 variant and not by random H1 variants. Nevertheless, in a cell population those nanodomains could be marked by different H1 variants. This could explain why at single-cell level we lost preferential co-localization of 'low-GC' H1s with H1.0 (compared to H1.4/H1X) while by ChIP-Seq data, mega-base domains of 'low-GC' H1 variants coincide. If those nanodomains were homogeneously marked by the same H1 variant in the cell population, we would observe differential enrichments between H1 variants belonging to the same GC cluster, even at the mega-base level. This apparent intra-population ambiguity may be indicating a structural role of 'low-GC' H1 variants and emphasizes the existing partial redundancy among certain H1 variants.

H1.2, H1.3 and H1.5 are highly enriched at the nuclear periphery in T47D cells but also in all cell lines analyzed **(Figure 1, Figure 5 A, B)**. Super-resolution microscopy revealed that these H1 variants form an adjacent layer to Lamina and highly co-localize with H3K9me2 **(Figure 3 A-C)**. H3K9me2 is not only a universal component of LADs, but also it is indispensable for peripheral heterochromatin anchoring to the nuclear lamina (Poleshko et al., 2019). Universal H1.2, H1.3 and H1.5 enrichment at nuclear periphery directly point to these H1 variants as conserved components of LADs, as has been described for H3K9me2. Furthermore, these H1 variants could be postulated as potential orchestrating factors for chromatin tethering to the lamina. Proper chromatin-lamina interactions are crucial to maintain chromatin dynamics (Briand and Collas, 2020; Chandra et al., 2015; Chang et al., 2022; Zheng et al., 2018). LADs detachment through Lamin B1 KO in human cells led to abnormal segregation of chromosome territories and A/B compartments, as well as global chromatin decompaction (Chang et al., 2022). Actually, we have shown that H1.2 depletion in T47D cells also led to a global chromatin decompaction **(Figure 4)**.

Interactions between the nuclear lamina and LADs are disrupted at early stages of mitosis and re-established upon mitotic exit. In general, mitosis involves large structural reorganization of chromatin (Imakaev et al., 2012) that is accompanied by eviction of multiple chromatin factors from DNA (Martínez-Balbás et al., 1995). On the other hand, factors that persist attached to chromatin, including multiple histone variants and histone modifications (Wang and Higgins, 2013), are suggested to act as spatial 'bookmarks'. This is the case of H3K9me2, which is reported to safeguard positional information of LADs through mitosis, through a phospho-methyl switch (H3K9me2S10p) (Poleshko et al., 2019). Indeed, we have found that interphasic 'low-GC' H1 variants persist more attached to chromatin during mitosis, compared to 'high-GC' ones **(Figure 2E, Figure 2-figure supplement 2, 3)**. Moreover, H1.3 and H1.5, which are highly associated to LADs in interphase, persist in the peripheral layer of mitotic chromosomes, showing an analogous profile to the one reported for H3K9me2 (Poleshko et al., 2019). H1.2 attachment to mitotic chromatin is regulated by phosphorylation at early mitotic

stages, but interestingly, H1.2 layer re-associates to the forming lamina upon mitotic exit. The strong similarities observed for H1.2, H1.3 and H1.5 with H3K9me2 in both interphase and mitosis suggest that these linker histones may also act as 3D positional 'bookmarks' of LADs.

We found that H1 variants may localize to nucleoli. Concretely, H1X and some phosphorylated H1s present different nucleolar distribution patterns (**Figure 3F**). H1X nucleolar enrichment has already been described in previous works (Mayor et al., 2015; Stoldt et al., 2007). In addition, other histone variants have been found at nucleoli, including testis-restricted H1T linker histone (Tani et al., 2016) or certain core histone variants (Jiang et al., 2021; Long et al., 2019; Pang et al., 2020). Importantly, nucleolar localization of H1X persists after inhibition of RNApol I by Actinomycin D **(Figure 3-figure supplement 1D)**, which was also reported previously (Stoldt et al., 2007). These observations might suggest a more structural role of H1X in nucleoli rather than a more functional or regulatory one. On the contrary, H1.2-pT165 and H1.4-pT146 seem to execute a functional role, as the nucleolar distribution of these post-translationally-modified H1 variants depends on functional nucleoli, with H1.4-pT146 being presumably associated to RNA pol I active transcription. The nucleolus is a membraneless organelle formed through liquid-liquid phase separation driven by multivalent interactions of its components (Lafontaine et al., 2021). Several molecular features are known drivers for phase separation, including highly intrinsically disordered regions (Shin and Brangwynne, 2017). Indeed, nucleolar proteome and specially proteins localized to the nucleolar rim are extremely disordered (Stenström et al., 2020). We found that nucleolar H1X is enriched, although not limited, at the nucleolar rim, adjacent to the inner side of NPM1 layer **(Figure 3E)**. Histone H1 proteins have a well-known highly disordered structure and have been shown to phase separate *in vitro* (Gibson et al., 2019; Shakya et al., 2020; Turner et al., 2018). However, the functional relevance of H1 variants as promotors of phase separation in living cells have not been explored.

Proteomic studies in four human cell lines demonstrated that almost 1/3 of the candidate H1.0-binding proteins localized to nucleolus and were related to nucleolar functionality (Kalashnikova et al., 2013). Remarkably, the experiments were performed by pull-down of exogenous, chimeric HaloTag-H1.0 protein. Importantly, direct H1.0 nucleolar localization or rRNA metabolism alterations upon H1.0 depletion were not reported. In contrast, our results show that H1.0 is depleted from nucleoli in all cell lines analyzed **(Figure 5A, B)**. We also checked that H1.0 does not redistribute to nucleoli upon H1X depletion in T47D cells (data not shown). Nevertheless, we cannot discard that H1.0 interacts with nucleolus-related proteins, as it can be enriched at perinucleolar heterochromatin or NADs, as observed in T47D cells.

We have explored how H1 variants depletion affect chromatin structure through super-resolution imaging of DNA **(Figure 4)**. In T47D cells, combined depletion of H1.2 and H1.4 (i.e. multiH1 KD) caused a global chromatin decompaction. This is in agreement with

previously generated ATAC-Seq experiments in these cells, which pointed to a genome-wide gain of chromatin accessibility. Accordingly, Hi-C data analysis in multiH1 KD cells also showed more de-compacted TAD structures (Serna-Pujol et al., 2022). In mice, multiple H1 variants deficiency have been also associated to chromatin decompaction (Willcockson et al., 2021; Yusufova et al., 2021). However, the differential contribution of individual H1 variants to chromatin structure has not been explored before. Interestingly, analysis of T47D single KDs revealed that single H1.2 depletion also led to chromatin decompaction, but not as pronounced as multiH1 KD. On the contrary, single depletion of H1.4 or H1X did not cause a significant alteration of chromatin structure. These observations suggest that the structural defects cannot be explained just for the total H1 reduction. Indeed, both H1.2 and H1.4 proteins contribution to total H1 content is the same in T47D, estimated to be 23-24% in each case (Sancho et al., 2008). Thus, H1 variant specific functionality, related to their differential genomic distribution seems to play a role. These results could support the putative structural function of H1.2 (and maybe also for the rest of 'low-GC' variants). In multiH1 KD cells, total H1 content is reduced ≈30% and chromatin decompaction is more drastic compared to single H1.2 depletion. Due to the fact that H1.2 and H1.4 occupy different genomic regions, the more drastic effects on decompaction in multiH1 KD cells seem to be due, at least in part, to the additive depletion of two H1 variants with non-redundant functions. In the whole, super-resolution microscopy of DNA enables us to decipher global compaction changes upon several H1 KDs conditions and revealed that H1 variants have specific roles in shaping genome architecture. Moreover, both the total H1 reduction but also the H1 variant repertoire have an impact on the global chromatin compaction homeostasis.

H1 complement is known to be heterogeneous among cell types. We have observed that H1X is expressed in all cell lines tested, as it was previously reported with H1.2 and H1.4 (Millán-Ariño et al., 2016). Interestingly, the simultaneous lack of H1.3 and H1.5 is found recurrently and seems to be mediated by DNA methylation (**Figure 5-figure supplement 1, 2**). On the contrary, whether H1 variants are universally distributed or display cell-type specific patterns is not well understood. H1 variants are thought to be specifically distributed among different cell lines, but this presumption comes from combining various pieces of evidence from different publications (Cao et al., 2013; Izzo et al., 2013; Li et al., 2012; Millán-Ariño et al., 2014; Morales-Torres et al., 2016). They mostly address the analysis of a single H1 variant in a particular model or cell line. Moreover, a comparative study of the distribution of a single H1 variant in different cell models has not been performed so far. In the whole, the direct comparison of these studies is biased by the different origin of the data and the varied methodologies used, which in many cases involve the over-expression of H1 variants.

We performed the first systematic analysis of six endogenous variants in different cancer cell lines. Our data unveils, for the first time, universal nuclear patterns exhibited by

specific H1 variants. Immunofluorescence experiments revealed that H1.2, H1.3 and H1.5 are universally enriched towards nuclear periphery. H1.0 and H1.4 are distributed throughout the whole nucleus but they show a more peripheral distribution in a subset of cell lines lacking H1.3 and H1.5 **(Figure 5)**. H1X is also distributed throughout the whole nucleus in all cell lines tested with a variable relative nucleolar enrichment. H1.0 and H1.4 re-distribution when H1.3 and H1.5 proteins are absent contrast to the behavior observed in T47D multiH1 KD. Upon multi-H1 KD, H1 variants distribution is overall robust, with no significant changes at the nuclear level (Serna-Pujol et al., 2022). These represent two different H1-compromised scenarios. In the first one, H1.3 and H1.5 silencing is intrinsically linked to the cell line identity. On the contrary, multiH1 KD cells represent an inducible H1.2 and H1.4 depletion, abnormal in T47D cells. Our results suggest that compensatory mechanisms between different H1 variants, in terms of distribution, may be limited when perturbing H1 levels but achieved when H1 repertoire is 'naturally' compromised.

In summary, our findings highlight the differential distribution of H1 variants within nuclear domains and their variant-specific role on chromatin. Moreover, we showed that H1 variants present a potentially more uniform distribution among cell lines than previously anticipated, particularly for certain variants.

## DATA AVAILABILITY STATEMENT

ChIP-Seq data of H1X in five different cancer cell lines have been deposited in NCBI's Gene Expression Omnibus (GEO) and is accessible through GEO Series accession number GSE236678. ChIP-Seq of H1.3 in T47D cells is available through the accession number GSE236878.

## SUPPLEMENTARY DATA

Supplementary Data are available online.


## ACKNOWLEDGEMENTS

We acknowledge Núria Serna for bioinformatics support on genomics data analysis, Pau Homs for assistance on some immunofluorescence quantifications, Stefany Montúfar and Núria Pell for assistance on immunoblot analysis of cell lines, and Carles Bonet for help with cell line conservation and laboratory managing. We acknowledge Generalitat de Catalunya and the European Social Fund for an AGAUR-FI predoctoral fellowship [to M.S.-P.].

## FUNDING

This work was supported by the Spanish Ministry of Science and Innovation [PID2020-112783GB-C21 to A.J.]. We also acknowledge the Generalitat de Catalunya Suport Grups de Recerca AGAUR 2017-SGR-597 to A.J. Funding for open access charge: Spanish Ministry of Science and Innovation.


## CONFLICT OF INTEREST

Authors declare no conflicts of interests.

## REFERENCES


Bersaglieri C, Kresoja-Rakic J, Gupta S, Bär D, Kuzyakiv R, Panatta M, Santoro R. 2022. Genome-wide maps of nucleolus interactions reveal distinct layers of repressive chromatin domains. *Nat Commun* **13**:1483. doi:10.1038/s41467-022-29146-2

Boyle S, Gilchrist S, Bridger JM, Mahy NL, Ellis JA, Bickmore WA. 2001. The spatial organization of human chromosomes within the nuclei of normal and emerin-mutant cells. *Hum Mol Genet* **10**:211–9. doi:10.1093/hmg/10.3.211

Briand N, Collas P. 2020. Lamina-associated domains: Peripheral matters and internal affairs. *Genome Biol* **21**:85. doi:10.1186/s13059-020-02003-5

Burger K, Mühl B, Harasim T, Rohrmoser M, Malamoussi A, Orban M, Kellner M, Gruber-Eber A, Kremmer E, Hölzel M, Eick D. 2010. Chemotherapeutic drugs inhibit ribosome biogenesis at various levels. *Journal of Biological Chemistry* **285**:12416–25. doi:10.1074/jbc.M109.074211

Cao K, Lailler N, Zhang Y, Kumar A, Uppal K, Liu Z, Lee EK, Wu H, Medrzycki M, Pan C, Ho PY, Cooper GP, Dong X, Bock C, Bouhassira EE, Fan Y. 2013. High-resolution mapping of H1 linker histone variants in embryonic stem cells. *PLoS Genet* **9**:e1003417. doi:10.1371/journal.pgen.1003417

Chandra T, Ewels PA, Schoenfelder S, Furlan-Magaril M, Wingett SW, Kirschner K, Thuret J-Y, Andrews S, Fraser P, Reik W. 2015. Global Reorganization of the Nuclear Landscape in Senescent Cells. *Cell Rep* **10**:471–483. doi:10.1016/j.celrep.2014.12.055

Chang L, Li M, Shao S, Li Chen, Ai S, Xue B, Hou Y, Zhang Y, Li R, Fan X, He A, Li Cheng, Sun Y. 2022. Nuclear peripheral chromatin-lamin B1 interaction is required for global integrity of chromatin architecture and dynamics in human cells. *Protein Cell* **13**:258–280. doi:10.1007/s13238-020-00794-8

Cremer T, Cremer C. 2001. Chromosome territories, nuclear architecture and gene regulation in mammalian cells. *Nat Rev Genet* **2**:292–301. doi:10.1038/35066075

Culley S, Tosheva KL, Matos Pereira P, Henriques R. 2018. SRRF: Universal live-cell super-resolution microscopy. *International Journal of Biochemistry and Cell Biology* **101**:74–79. doi:10.1016/j.biocel.2018.05.014

Dillinger S, Straub T, Nemeth A. 2017. Nucleolus association of chromosomal domains is largely maintained in cellular senescence despite massive nuclear reorganisation. *PLoS One* **12**:e0178821. doi:10.1371/journal.pone.0178821

Dixon JR, Selvaraj S, Yue F, Kim A, Li Y, Shen Y, Hu M, Liu JS, Ren B. 2012. Topological domains in mammalian genomes identified by analysis of chromatin interactions. *Nature* **485**:376–380. doi:10.1038/nature11082

Karolchik D, Hinrichs A, Furey TS, Roskin KM, W Sugnet C, Haussler D, Kent WJ. 2004. The UCSC Table Browser data retrieval tool. *Nucleic Acids Res* **32**:D493-6. doi:10.1093/nar/gkh103

Fyodorov D V, Zhou B-R, Skoultchi AI, Bai Y. 2018. Emerging roles of linker histones in regulating chromatin structure and function. *Nat Rev Mol Cell Biol* **19**:192–206. doi:10.1038/nrm.2017.94

Geeven G, Zhu Y, Kim BJ, Bartholdy BA, Yang SM, Macfarlan TS, Gifford WD, Pfaff SL, Verstegen MJAM, Pinto H, Vermunt MW, Creyghton MP, Wijchers PJ, Stamatoyannopoulos JA, Skoultchi AI, de Laat W. 2015. Local compartment changes and regulatory landscape alterations in histone H1-depleted cells. *Genome Biol* **16**:289. doi:10.1186/s13059-015-0857-0

Gibson BA, Doolittle LK, Schneider MWG, Jensen LE, Gamarra N, Henry L, Gerlich DW, Redding S, Rosen MK. 2019. Organization of Chromatin by Intrinsic and Regulated Phase Separation. *Cell* **179**:470–484. doi:10.1016/j.cell.2019.08.037

Girelli G, Custodio J, Kallas T, Agostini F, Wernersson E, Spanjaard B, Mota A, Kolbeinsdottir S, Gelali E, Crosetto N, Bienko M. 2020. GPSeq reveals the radial organization of chromatin in the cell nucleus. *Nat Biotechnol* **38**:1184–1193. doi:10.1038/s41587-020-0519-y

Guelen L, Pagie L, Brasset E, Meuleman W, Faza MB, Talhout W, Eussen BH, De Klein A, Wessels L, De Laat W, Van Steensel B. 2008. Domain organization of human chromosomes revealed by mapping of nuclear lamina interactions. *Nature* **453**:948–51. doi:10.1038/nature06947

Gustafsson N, Culley S, Ashdown G, Owen DM, Pereira PM, Henriques R. 2016. Fast live-cell conventional fluorophore nanoscopy with ImageJ through super-resolution radial fluctuations. *Nat Commun* **7**:12471. doi:10.1038/ncomms12471

Harr JC, Luperchio TR, Wong X, Cohen E, Wheelan SJ, Reddy KL. 2015. Directed targeting of chromatin to the nuclear lamina is mediated by chromatin state and A-type lamins. *Journal of Cell Biology* **208**:33–52. doi:10.1083/jcb.201405110

Imakaev M, Fudenberg G, McCord RP, Naumova N, Goloborodko A, Lajoie BR, Dekker J, Mirny LA. 2012. Iterative correction of Hi-C data reveals hallmarks of chromosome organization. *Nat Methods* **9**:999–1003. doi:10.1038/nmeth.2148

Izquierdo-Bouldstridge A, Bustillos A, Bonet-Costa C, Aribau-Miralbés P, García-Gomis D, Dabad M, Esteve-Codina A, Pascual-Reguant L, Peiró S, Esteller M, Murtha M, Millán-Ariño L, Jordan A. 2017. Histone H1 depletion triggers an interferon response in cancer cells via activation of heterochromatic repeats. *Nucleic Acids Res* **45**:11622–11642. doi:10.1093/nar/gkx746

Izzo A, Kamieniarz-Gdula K, Ramírez F, Noureen N, Kind J, Manke T, VanSteensel B, Schneider R. 2013. The Genomic Landscape of the Somatic Linker Histone Subtypes H1.1 to H1.5 in Human Cells. *Cell Rep* **3**:2142–54. doi:10.1016/j.celrep.2013.05.003

Jiang X, Wen J, Paver E, Wu Y, Sun G, Bullman A, Dahlstrom JE, Tremethick DJ, Soboleva TA. 2021. H2A.B is a cancer/testis factor involved in the activation of ribosome biogenesis in Hodgkin lymphoma. *EMBO Rep* **22**:e52462. doi:10.15252/embr.202152462

Jost KL, Bertulat B, Cardoso MC. 2012. Heterochromatin and gene positioning: Inside, outside, any side? *Chromosoma* **121**:555–563. doi:10.1007/s00412-012-0389-2

Kalashnikova AA, Winkler DD, McBryant SJ, Henderson RK, Herman JA, DeLuca JG, Luger K, Prenni JE, Hansen JC. 2013. Linker histone H1.0 interacts with an extensive network of proteins found in the nucleolus. *Nucleic Acids Res* **41**:4026–4035. doi:10.1093/nar/gkt104

Kind J, Pagie L, Ortabozkoyun H, Boyle S, De Vries SS, Janssen H, Amendola M, Nolen LD, Bickmore WA, Van Steensel B. 2013. Single-cell dynamics of genome-nuclear lamina interactions. *Cell* **153**:178–92. doi:10.1016/j.cell.2013.02.028

Lafontaine DLJ, Riback JA, Bascetin R, Brangwynne CP. 2021. The nucleolus as a multiphase liquid condensate. *Nat Rev Mol Cell Biol* **22**:165–182. doi:https://doi.org/10.1038/s41580-020-0272-6

Lennox RW, Cohen LH. 1983. The histone H1 complements of dividing and nondividing cells of the mouse. *Journal of Biological Chemistry* **258**:262–8. doi:10.1016/s0021-9258(18)33251-4

Li JY, Patterson M, Mikkola HKA, Lowry WE, Kurdistani SK. 2012. Dynamic Distribution of Linker Histone H1.5 in Cellular Differentiation. *PLoS Genet* **8**:e1002879. doi:10.1371/journal.pgen.1002879

Lieberman-Aiden E, Van Berkum NL, Williams L, Imakaev M, Ragoczy T, Telling A, Amit I, Lajoie BR, Sabo PJ, Dorschner MO, Sandstrom R, Bernstein B, Bender MA, Groudine M, Gnirke A, Stamatoyannopoulos J, Mirny LA, Lander ES, Dekker J. 2009. Comprehensive mapping of long-range interactions reveals folding principles of the human genome. *Science (1979)* **326**:289–293. doi:10.1126/science.1181369

Long M, Sun X, Shi W, Yanru A, Leung STC, Ding D, Cheema MS, MacPherson N, Nelson CJ, Ausio J, Yan Y, Ishibashi T. 2019. A novel histone H4 variant H4G regulates rDNA transcription in breast cancer. *Nucleic Acids Res* **47**:8399–8409. doi:10.1093/nar/gkz547

Martin L, Vicario C, Castells-García Á, Lakadamyali M, Neguembor MV, Cosma MP. 2021. A protocol to quantify chromatin compaction with confocal and super-resolution microscopy in cultured cells. *STAR Protoc* **2**:100865. doi:10.1016/j.xpro.2021.100865

Martínez-Balbás MA, Dey A, Rabindran SK, Ozato K, Wu C. 1995. Displacement of sequence-specific transcription factors from mitotic chromatin. *Cell* **83**:29–38. doi:10.1016/0092-8674(95)90231-7

Martire S, Banaszynski LA. 2020. The roles of histone variants in fine-tuning chromatin organization and function. *Nat Rev Mol Cell Biol* **21**:522–541. doi:10.1038/s41580-020-0262-8

Mayor R, Izquierdo-Bouldstridge A, Millán-Ariño L, Bustillos A, Sampaio C, Luque N, Jordan A. 2015. Genome distribution of replication-independent histone H1 variants shows H1.0 associated with nucleolar domains and H1X associated with RNA polymerase II-enriched regions. *Journal of Biological Chemistry* **290**:7474–7491. doi:10.1074/jbc.M114.617324

Meergans T, Albig W, Doenecke D. 1997. Varied expression patterns of human H1 histone genes in different cell lines. *DNA Cell Biol* **16**:1041–1049. doi:10.1089/dna.1997.16.1041

Millán-Ariño L, Islam ABMMK, Izquierdo-Bouldstridge A, Mayor R, Terme JM, Luque N, Sancho M, López-Bigas N, Jordan A. 2014. Mapping of six somatic linker histone H1 variants in human breast cancer cells uncovers specific features of H1.2. *Nucleic Acids Res* **42**:4474–4493. doi:10.1093/nar/gku079

Millán-Ariño L, Izquierdo-Bouldstridge A, Jordan A. 2016. Specificities and genomic distribution of somatic mammalian histone H1 subtypes. *Biochim Biophys Acta Gene Regul Mech* **1859**:510–519. doi:10.1016/j.bbagrm.2015.10.013

Morales-Torres C, Biran A, Burney MJ, Patel H, Henser-Brownhill T, Cohen AHS, Li Y, Ben-Hamo R, Nye E, Spencer-Dene B, Chakravarty P, Efroni S, Matthews N, Misteli T, Meshorer E, Scaffidi P. 2016. The linker histone H1.0 generates epigenetic and functional intratumor heterogeneity. *Science (1979)* **353**:aaf1644. doi:10.1126/science.aaf1644

Navarro Gonzalez J, Zweig AS, Speir ML, Schmelter D, Rosenbloom KR, Raney BJ, Powell CC, Nassar LR, Maulding ND, Lee CM, Lee BT, Hinrichs AS, Fyfe AC, Fernandes JD, Diekhans M, Clawson H, Casper J, Benet-Pagès A, Barber GP, Haussler D, Kuhn RM, Haeussler M, Kent WJ. 2021. The UCSC Genome Browser database: 2021 update. *Nucleic Acids Res* **49**:D1046–D1057. doi:10.1093/nar/gkaa1070

Neguembor MV, Martin L, Castells-García Á, Gómez-García PA, Vicario C, Carnevali D, AlHaj Abed J, Granados A, Sebastian-Perez R, Sottile F, Solon J, Wu C ting, Lakadamyali M, Cosma MP. 2021. Transcription-mediated supercoiling regulates genome folding and loop formation. *Mol Cell* **81**:3065–3081. doi:10.1016/j.molcel.2021.06.009

Nemeth A, Conesa A, Santoyo-Lopez J, Medina I, Montaner D, Peterfia B, Solovei I, Cremer T, Dopazo J, Langst G. 2010. Initial genomics of the human nucleolus. *PLoS Genet* **6**:e1000889. doi:10.1371/journal.pgen.1000889

Nora EP, Lajoie BR, Schulz EG, Giorgetti L, Okamoto I, Servant N, Piolot T, Van Berkum NL, Meisig J, Sedat J, Gribnau J, Barillot E, Blüthgen N, Dekker J, Heard E. 2012. Spatial partitioning of the regulatory landscape of the X-inactivation centre. *Nature* **485**:381–385. doi:10.1038/nature11049

Pang MYH, Sun X, Ausió J, Ishibashi T. 2020. Histone H4 variant, H4G, drives ribosomal RNA transcription and breast cancer cell proliferation by loosening nucleolar chromatin structure. *J Cell Physiol* **235**:9601–9608. doi:10.1002/jcp.29770

Parseghian MH, Hamkalo BA. 2001. A compendium of the histone H1 family of somatic subtypes: An elusive cast of characters and their characteristics. *Biochemistry and Cell Biology* **79**:289–304.

Peng T, Hou Y, Meng H, Cao Y, Wang X, Jia L, Chen Q, Zheng Y, Sun Y, Chen H, Li T, Li C. 2023. Mapping nucleolus-associated chromatin interactions using nucleolus Hi-C reveals pattern of heterochromatin interactions. *Nat Commun* **14**. doi:10.1038/s41467-023-36021-1

Piña B, Suau P. 1987. Changes in the proportions of histone H1° subtypes in brain cortical neurons. *FEBS Lett* **210**:161–164. doi:10.1016/0014-5793(87)81328-5

Poleshko A, Smith CL, Nguyen SC, Sivaramakrishnan P, Wong KG, Murray JI, Lakadamyali M, Joyce EF, Jain R, Epstein JA. 2019. H3K9me2 orchestrates inheritance of spatial positioning of peripheral heterochromatin through mitosis. *Elife* **8**:e49278. doi:10.7554/eLife.49278

Quinlan AR, Hall IM. 2010. BEDTools: A flexible suite of utilities for comparing genomic features. *Bioinformatics* **26**:841–2. doi:10.1093/bioinformatics/btq033

Reinhold WC, Varma S, Sunshine M, Elloumi F, Ofori-Atta K, Lee S, Trepel JB, Meltzer PS, Doroshow JH, Pommier Y. 2019. RNA sequencing of the NCI-60: Integration into CellMiner and CellMiner CDB. *Cancer Res* **79**:3514–3524. doi:10.1158/0008-5472.CAN-18-2047

Ricci MA, Manzo C, García-Parajo MF, Lakadamyali M, Cosma MP. 2015. Chromatin fibers are formed by heterogeneous groups of nucleosomes in vivo. *Cell* **160**:1145–58. doi:10.1016/j.cell.2015.01.054

Sancho M, Diani E, Beato M, Jordan A. 2008. Depletion of human histone H1 variants uncovers specific roles in gene expression and cell growth. *PLoS Genet* **4**:e1000227. doi:10.1371/journal.pgen.1000227

Serna-Pujol N, Salinas-Pena M, Mugianesi F, Le Dily F, Marti-Renom MA, Jordan A. 2022. Coordinated changes in gene expression, H1 variant distribution and genome 3D conformation in response to H1 depletion. *Nucleic Acids Res* **50**:3892–3910. doi:10.1093/nar/gkac226

Serna-Pujol N, Salinas-Pena M, Mugianesi F, Lopez-Anguita N, Torrent-Llagostera F, Izquierdo-Bouldstridge A, Marti-Renom MA, Jordan A. 2021. TADs enriched in histone H1.2 strongly overlap with the B compartment, inaccessible chromatin and AT-rich Giemsa bands. *FEBS J* **288**:1989–2013. doi:10.1111/febs.15549

Sexton T, Yaffe E, Kenigsberg E, Bantignies F, Leblanc B, Hoichman M, Parrinello H, Tanay A, Cavalli G. 2012. Three-dimensional folding and functional organization principles of the Drosophila genome. *Cell* **148**:458–472. doi:10.1016/j.cell.2012.01.010

Shakya A, Park S, Rana N, King JT. 2020. Liquid-Liquid Phase Separation of Histone Proteins in Cells: Role in Chromatin Organization. *Biophys J* **118**:753–764. doi:10.1016/j.bpj.2019.12.022

Shin Y, Brangwynne CP. 2017. Liquid phase condensation in cell physiology and disease. *Science (1979)* **357**:eaaf4382. doi:10.1126/science.aaf4382

Solovei I, Thanisch K, Feodorova Y. 2016. How to rule the nucleus: divide et impera. *Curr Opin Cell Biol* **40**:47–59. doi:10.1016/j.ceb.2016.02.014

Stenström L, Mahdessian D, Gnann C, Cesnik AJ, Ouyang W, Leonetti MD, Uhlén M, Cuylen-Haering S, Thul PJ, Lundberg E. 2020. Mapping the nucleolar proteome reveals a spatiotemporal organization related to intrinsic protein disorder. *Mol Syst Biol* **16**:e9469. doi:10.15252/msb.20209469

Stoldt S, Wenzel D, Schulze E, Doenecke D, Happel N. 2007. G1 phase-dependent nucleolar accumulation of human histone H1x. *Biol Cell* **99**:541–552. doi:10.1042/bc20060117

Tani R, Hayakawa K, Tanaka S, Shiota K. 2016. Linker histone variant H1T targets rDNA repeats. *Epigenetics* **11**:288–302. doi:10.1080/15592294.2016.1159369

Terme JM, Sesé B, Millán-Ariño L, Mayor R, Belmonte Izpisúa JC, Barrero MJ, Jordan A. 2011. Histone H1 variants are differentially expressed and incorporated into chromatin during differentiation and reprogramming to pluripotency. *Journal of Biological Chemistry* **286**:35347–35357. doi:10.1074/jbc.M111.281923

Turner AL, Watson M, Wilkins OG, Cato L, Travers A, Thomas JO, Stott K. 2018. Highly disordered histone H1−DNA model complexes and their condensates. *Proc Natl Acad Sci U S A* **115**:11964–11969. doi:10.1073/pnas.1805943115

Wang F, Higgins JMG. 2013. Histone modifications and mitosis: countermarks, landmarks, and bookmarks. *Trends Cell Biol* **23**:175–84. doi:10.1016/j.tcb.2012.11.005

Willcockson MA, Healton SE, Weiss CN, Bartholdy BA, Botbol Y, Mishra LN, Sidhwani DS, Wilson TJ, Pinto HB, Maron MI, Skalina KA, Toro LN, Zhao J, Lee CH, Hou H, Yusufova N, Meydan C, Osunsade A, David Y, Cesarman E, Melnick AM, Sidoli S, Garcia BA, Edelmann W, Macian F, Skoultchi AI. 2021. H1 histones control the epigenetic landscape by local chromatin compaction. *Nature* **589**:293–298. doi:10.1038/s41586-020-3032-z

Yusufova N, Kloetgen A, Teater M, Osunsade A, Camarillo JM, Chin CR, Doane AS, Venters BJ, Portillo-Ledesma S, Conway J, Phillip JM, Elemento O, Scott DW, Béguelin W, Licht JD, Kelleher NL, Staudt LM, Skoultchi AI, Keogh MC, Apostolou E, Mason CE, Imielinski M, Schlick T, David Y, Tsirigos A, Allis CD, Soshnev AA, Cesarman E, Melnick AM. 2021. Histone H1 loss drives lymphoma by disrupting 3D chromatin architecture. *Nature* **589**:299–305. doi:10.1038/s41586-020-3017-y

Zheng X, Hu J, Yue S, Kristiani L, Kim M, Sauria M, Taylor J, Kim Y, Zheng Y. 2018. Lamins Organize the Global Three-Dimensional Genome from the Nuclear Periphery. *Mol Cell* **71**:802–815. doi:10.1016/j.molcel.2018.05.017

Zheng Y, John S, Pesavento JJ, Schultz-Norton JR, Schiltz RL, Baek S, Nardulli AM, Hager GL, Kelleher NL, Mizzen CA. 2010. Histone H1 phosphorylation is associated with transcription by RNA polymerases I and II. *Journal of Cell Biology* **189**:407–415. doi:10.1083/jcb.201001148

## FIGURE LEGENDS

**Figure 1. H1 variants are differentially enriched towards the nuclear periphery in T47D cells. A)** Confocal immunofluorescence of H1 variants (green) and DNA staining (blue). Bottom panels show the intensity profiles of H1 variants and DNA along the arrows depicted in the upper panel. Scale bar: 5µm. **B)** Example of one cell stained with H1.3 antibody in which four sections of an equivalent area and convergent to the nuclear center are shown. Sections are named A1 to A4, from the more peripheral section to the more central one. H1 variants immunofluorescence intensity were measured in each area and expressed as percentage. **C)** Quantifications of H1 variants using the segmentation illustrated in (B), where n=30 cells/condition were quantified, and data was represented in violin plots. Statistical differences between A1-A2, A2-A3 and A3-A4 for H1.0 and H1.4 are supported by paired t-test (***) p-value<0.001; (**) p-value<0.01; (ns/non-significant) p-value>0.05. **D)** H1 variants Input-subtracted ChIP-Seq median abundance per chromosome. Y-axis annotation indicated median %GC content per chromosome and their nuclear positions according to (Boyle et al., 2001; Girelli et al., 2020).

**Figure 2. Super-resolution imaging shows that H1 variants occupy different regions in single-cells. A)** SRRF images of H1 variants (green) and DNA (red). Bottom-left Insets show the Reference confocal image in each case. Scale bar: 2µm. **B)** Percentage of co-localized pixels between H1 variants and DNA by SRRF imaging. n=20 cells/condition were quantified and values distribution were represented as violin plots. **C)** SRRF images of H1 variants (green) and H1.0 (red). Bottom-left Insets show the Reference confocal image in each case. In the bottom panel, the highlighted zoom-in insets at confocal (reference) or SRRF resolutions are shown. Scale bar: 2µm, scale bar in zoom-in insets: 200nm. **D)** Percentage of colocalized pixels of H1 variants with H1.0 by SRRF imaging. n=20 cells/condition were quantified and values distribution were represented as violin plots. **E)** Immunofluorescence of H1 variants (green) and DNA (blue) during metaphase. As H1.2 and H1.4 signal was not detected during metaphase (see main text and **Figure 2-figure supplement 2 and 3**), antibodies recognizing specific phosphorylations of these variants were used. To see H1 variants profiles along mitosis progression, see **Figure 2-figure supplement 2 and 3**. Scale bar: 5µm.

**Figure 3. H1 variants presence within LADs and nucleoli. A)** Confocal (left) and super-resolution (right) images of a T47D cells stained for H1.2, H1.3 or H1.5 (in green) and Lamin A (in red) obtained using SRRF. Full nuclei (upper panel) and zoomed views of nuclear periphery (bottom panel) are shown. Scale bars: 2 µm (upper panel) and 200nm (bottom panel). Three representative cells are shown for each H1 variant. **B)** Pearson correlation coefficient (r) of H1 variants and H3K9me2 co-immunostaining signal. r values distribution in n=50 cells/condition are shown. Representative immunofluorescence images of H1 variants and H3K9me2 are shown in **Figure 3-figure supplement 1A**. Scale bar: 5µm. **C)** H1.3 and H3K9me2 immunofluorescence at confocal

(reference) and super-resolution (SRRF) level. A zoom-in inset of the peripheral layer formed by both H1.3 and H3K9me3 is shown. Scaler bar: 2µm. **D)** Boxplots show the Input-subtracted H1 variants ChIP-Seq abundance within regions exclusively defined as NADs (NAD only) or LADs (LAD only) and those genomic segments defined as both NADs and LADs (NAD/LAD). A compartment regions are included as a reference. NADs coordinates were extracted from (Peng et al., 2023). **E)** Representative SRRF image of H1X, NPM1 and DNA. Zoom-in highlights the H1X nucleolar layer. Scale bar: 2µm. Scale bar in zoom-in: 0.2µm. **F)** Immunofluorescence of H1X, H1.2-pT165 or H1.4-pT146, Nucleophosmin (NPM1) and DNA. Insets show a zoom-in of a single nucleolus. Scale bar: 2µm. Three representative cells are shown for each H1.

**Figure 4. Chromatin structural changes upon H1 depletion. A)** Representative SRRF images of DNA staining in the different H1 KD conditions indicated (multiH1, H1.2, H1.4 and H1X Dox-inducible shRNAs). In the bottom panels, a zoom-in inset is shown to appreciate DNA pattern in both Untreated and Dox conditions. Scale bar: 5µm (full nucleus) and 500nm (zoom-in). **B)** DNA-free areas percentage quantification in the different H1 KDs. n=20 cells/condition were quantified and the boxplot were constructed with the 20 average values in each condition. Statistical differences between Untreated and Dox-treated conditions are supported by paired-t-test. (***) p-value < 0.001; (ns/non-significant) p-value > 0.05. Additional representative images and full quantification are shown in **Figure 4-figure supplement 1**.

**Figure 5. Nuclear distribution of H1 variants across multiple human cell lines. A)** Immunofluorescence analysis of H1 variants (green) with DNA staining (blue) in different cancer cell lines. Merged images are shown. H1.3 and H1.0 grids in HeLa cells are empty, as HeLa cells do not express these variants. Tumoral origin of the cell lines is indicated. Scale bar: 5µm. **B)** Immunofluorescence analysis of H1 variants (green) with DNA staining (blue) in cell lines lacking H1.3 and H1.5. Merged images are shown. Tumoral origin of the cell lines is indicated. Scale bar: 5µm. **C)** H1.4 and H1.0 show a more peripheral distribution in cell lines with a compromised H1 repertoire. Numbers correspond to Peripheral Index value in each cell line and color-coded as indicated. Each nucleus was divided into four equivalent sections A1-A4 and immunofluorescence signal of H1.4 or H1.0 was quantified. Peripheral index was defined as the ratio between Average value in A1 peripheral section and A4 central section. **D)** Immunofluorescence of H1X (green), nucleolar marker NPM1 (magenta) and DNA staining (blue). Merged images are shown. Insets show a zoom-in of a single nucleolus. Bottom panel includes cell lines lacking H1.3 and H1.5. Cell line origin is indicated. Scale bar: 5µm. **E)** Boxplots show the H1X Input-subtracted ChIP-Seq signal at eight groups of Giemsa bands in six different cancer cell lines. G-bands groups were defined according to (Serna-Pujol et al., 2021) (see Methods).

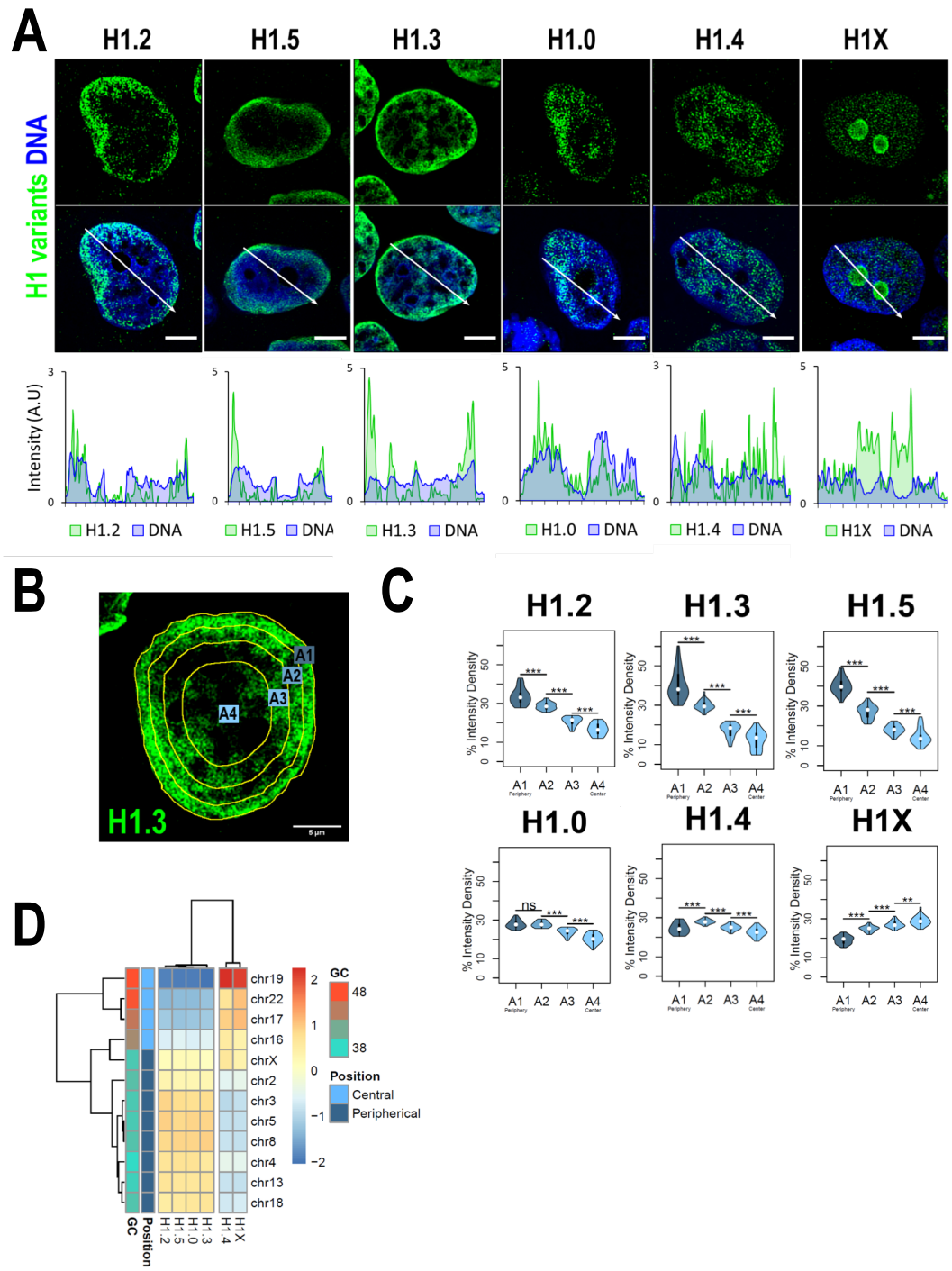
A
H1.2
H1.5
H1.3
H1.0
H1.4
H1X
H1 variants DNA
Intensity (A.U)
H1.2 DNA
H1.5 DNA
H1.3 DNA
H1.0 DNA
H1.4 DNA
H1X DNA
B
A1
A2
A3
A4
H1.3
C
% Intensity Density
A1 A2 A3 A4
D
chr19
chr22
chr17
chr16
chrX
chr2
chr3
chr5
chr8
chr4
chr13
chr18
GC
Position
H1.2
H1.5
H1.0
H1.3
H1.4
H1X
Central
Peripherical

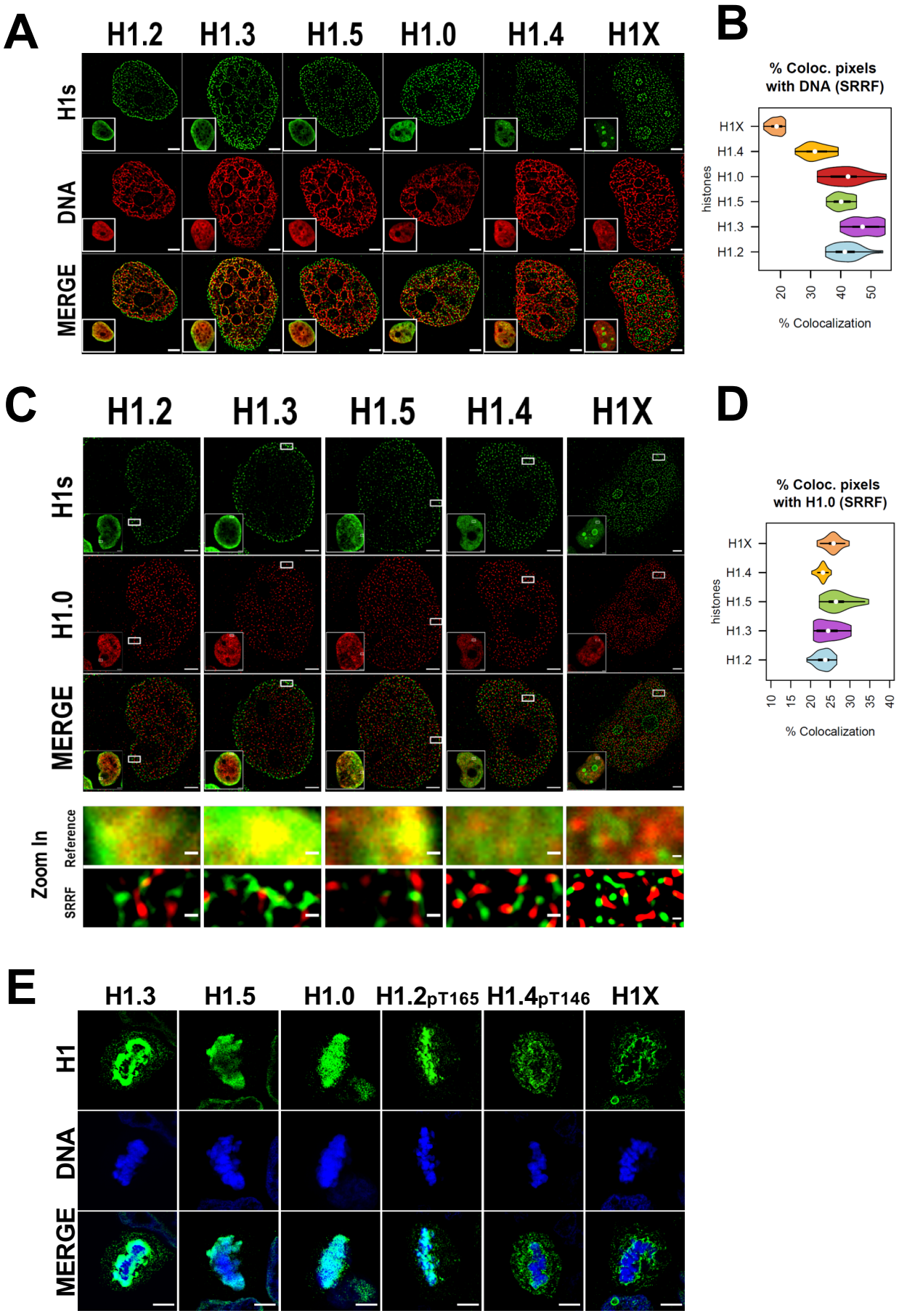
A
H1.2
H1.3
H1.5
H1.0
H1.4
H1X
H1s
DNA
MERGE
B
% Coloc. pixels with DNA (SRRF)
H1X
H1.4
H1.0
H1.5
H1.3
H1.2
histones
20
30
40
50
% Colocalization
C
H1.2
H1.3
H1.5
H1.4
H1X
H1s
H1.0
MERGE
Zoom In
Reference
SRRF
D
% Coloc. pixels with H1.0 (SRRF)
H1X
H1.4
H1.5
H1.3
H1.2
histones
10
15
20
25
30
35
40
% Colocalization
E
H1.3
H1.5
H1.0
H1.2pT165
H1.4pT146
H1X
H1
DNA
MERGE

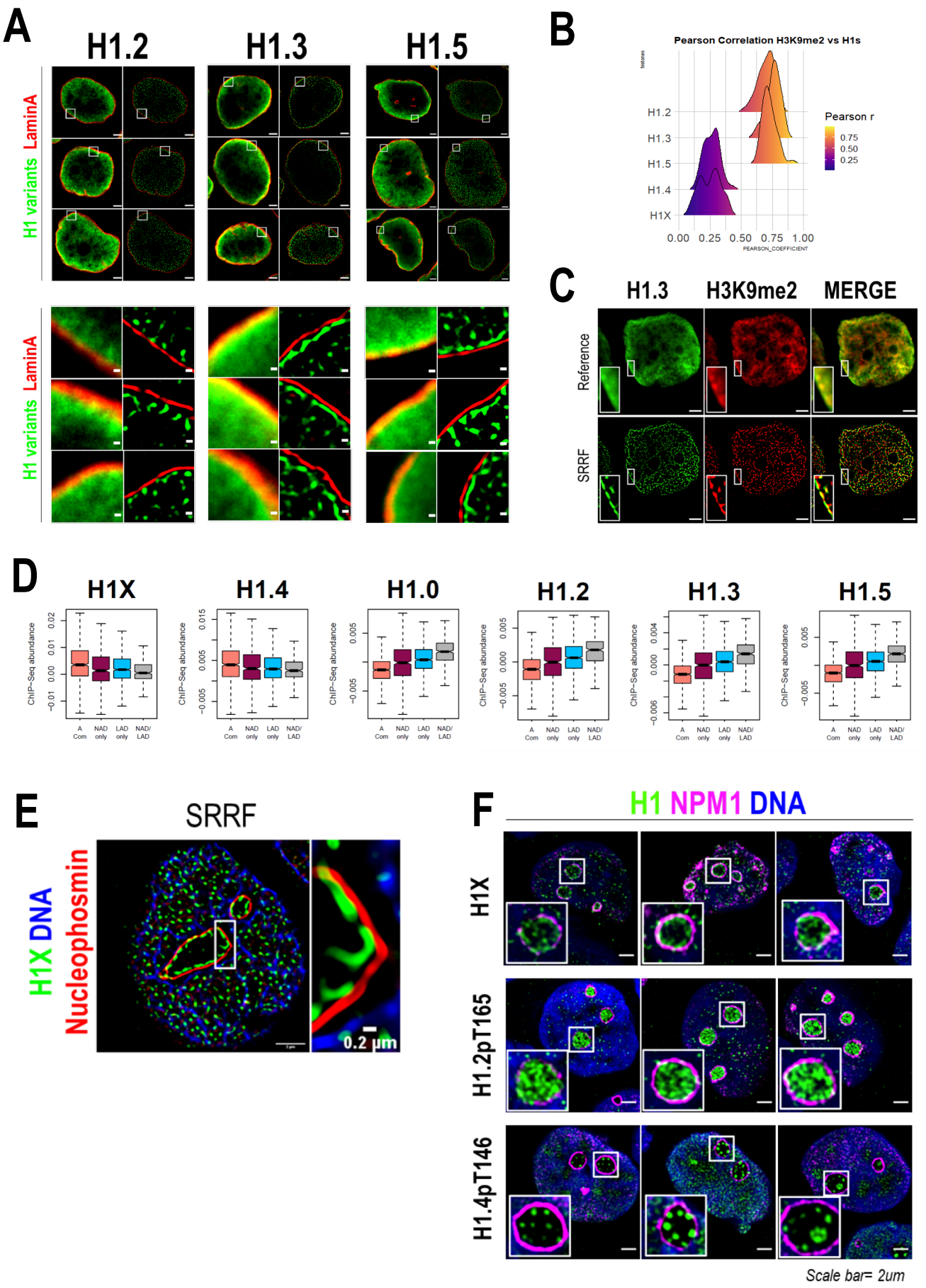
A
H1.2
H1.3
H1.5
H1 variants
LaminA
B
Pearson Correlation H3K9me2 vs H1s
H1.2
H1.3
H1.5
H1.4
H1X
Pearson r
0.75
0.50
0.25
0.00 0.25 0.50 0.75 1.00
PEARSON_COEFFICIENT
C
H1.3
H3K9me2
MERGE
Reference
SRRF
D
H1X
H1.4
H1.0
H1.2
H1.3
H1.5
ChIP-Seq abundance
A Com
NAD only
LAD only
NAD/ LAD
E
SRRF
H1X DNA
Nucleophosmin
0.2 µm
F
H1 NPM1 DNA
H1X
H1.2pT165
H1.4pT146
Scale bar= 2um

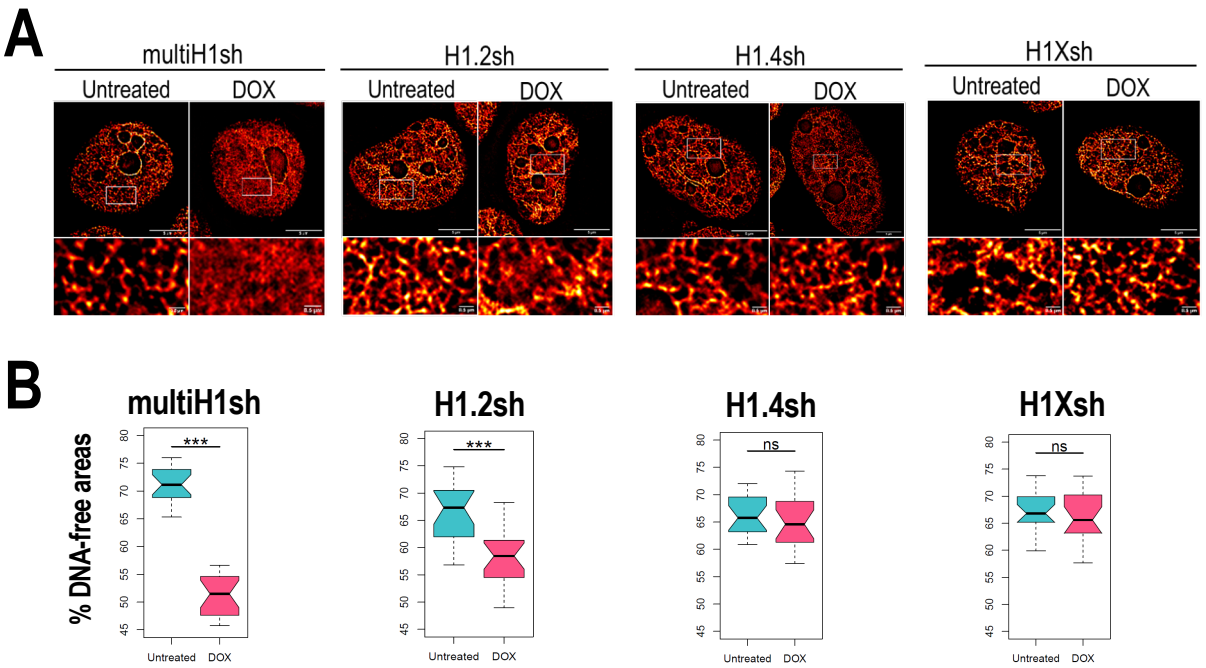
A
multiH1sh
H1.2sh
H1.4sh
H1Xsh
Untreated
DOX
B
multiH1sh
H1.2sh
H1.4sh
H1Xsh
% DNA-free areas
***
ns
Untreated
DOX

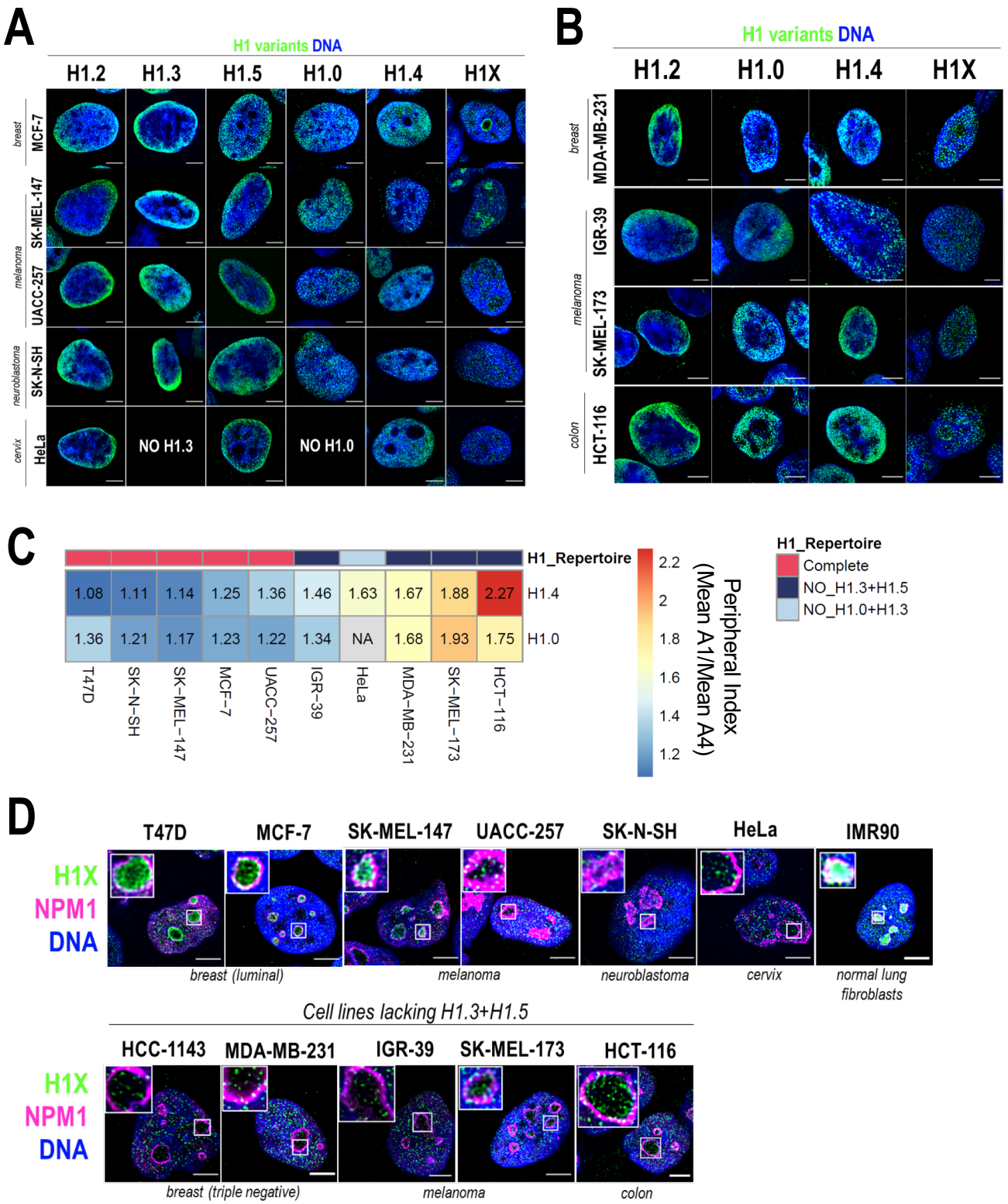
A
H1 variants DNA
H1.2
H1.3
H1.5
H1.0
H1.4
H1X
breast
MCF-7
melanoma
SK-MEL-147
UACC-257
neuroblastoma
SK-N-SH
cervix
HeLa
NO H1.3
NO H1.0
B
H1 variants DNA
H1.2
H1.0
H1.4
H1X
breast
MDA-MB-231
melanoma
IGR-39
SK-MEL-173
colon
HCT-116
C
H1_Repertoire
H1.4
H1.0
1.08 1.11 1.14 1.25 1.36 1.46 1.63 1.67 1.88 2.27
1.36 1.21 1.17 1.23 1.22 1.34 NA 1.68 1.93 1.75
T47D
SK-N-SH
SK-MEL-147
MCF-7
UACC-257
IGR-39
HeLa
MDA-MB-231
SK-MEL-173
HCT-116
2.2
2
1.8
1.6
1.4
1.2
Peripheral Index
(Mean A1/Mean A4)
H1_Repertoire
Complete
NO_H1.3+H1.5
NO_H1.0+H1.3
D
T47D
MCF-7
SK-MEL-147
UACC-257
SK-N-SH
HeLa
IMR90
H1X
NPM1
DNA
breast (luminal)
melanoma
neuroblastoma
cervix
normal lung fibroblasts
Cell lines lacking H1.3+H1.5
HCC-1143
MDA-MB-231
IGR-39
SK-MEL-173
HCT-116
H1X
NPM1
DNA
breast (triple negative)
melanoma
colon
E
Input-subtracted ChIP-Seq signal
T47D
SK-MEL-147
MCF-7
SK-N-SH
HeLa
HCT-116
1 2 3 4 25 50 75 100
Gneg
Gpos